Characterization of Dislocations in hcp 4He by Torsional Oscillator and Thermal Conductivity Measurements

Document Version
Final published version

Characterization of Dislocations in hcp ⁴He by Torsional Oscillator and Thermal Conductivity Measurements

M. Yu. Brazhnikov[1,2] · Y. M. Mukharsky[3] · A. I. Golov[1]

© The Author(s) 2022

Abstract

We apply two complementary techniques for the characterization of mobile dislocations in samples of hcp ⁴He with the concentration of ³He $\sim 3 \times 10^{-7}$, grown by the blocked capillary method at molar volume 19.5 cm³ mol⁻¹, before and after annealing at temperatures 1.8–2.0 K, and also after work hardening by high-amplitude twisting at 0.03 K and successive recovery at 0.5–1.0 K. The first technique relies on the elastic response of solid helium to oscillatory twisting at frequencies 161 Hz and 931 Hz at temperatures below 1 K, where this response is affected by the presence of mobile dislocations with variable amounts of trapped ³He impurities. Monitoring the non-equilibrium amplitude dependence after moderate forcing allows to compute the length distribution $n(L)$ of mobile dislocations (Iwasa in J Low Temp Phys 171:30, 2013; Fefferman et al. in Phys Rev B 89:014105, 2014). We also test methods of determining $n(L)$ from the equilibrium temperature dependence of either real or imaginary part of the shear modulus at small strain amplitudes, based on the values of the damping force measured by Fefferman et al. [2]. The second technique utilizes measurements of thermal conductivity at temperatures below 0.4 K, i.e., of the dislocation-limited mean free path of thermal transverse phonons (Greenberg and Armstrong in Phys Rev B 20:1049, 1979; Armstrong et al. in Phys Rev B 20:1061, 1979). During a prolonged AC-twisting at a high amplitude of strain exceeding the yield stress, long dislocations disappear being replaced by many short ones which remain mobile. However, upon stopping this twisting, the majority of dislocations become immobilized until the sample is warmed up above 0.5 K to speed-up the recovery of dislocations to their mobile state (Day et al. in Phys Rev B 79:214524, 2009; Beamish and Franck in Phys Rev B 26:6104, 1982). This is different from the immobilization of dislocations by trapped ³He impurities, routinely observed at smaller strain amplitudes, which is characterized by much shorter relaxation times to effectively un-trap ³He atoms and make dislocations mobile again. We investigated the dynamics of the recovery of cold-worked samples, during which short segments quickly disappear, while the longest one appear after longer annealing times; the activation energy was estimated to be 22 K—pointing at the thermal vacancy-assisted process. A complementary characterization by the scattering

---

Extended author information available on the last page of the article

rate of thermal transverse phonons off crystalline defects rules out non-interacting mobile dislocations as the dominant scatterer. The main conclusion is that while many properties of the sample are consistent with the theory of Granato and Lücke of isolated gliding dislocations (Granato and Lücke in J Appl Phys 27:583, 1956), several observations at low temperatures (^{3}He-independent immobilization of dislocations after stopping high-amplitude twisting, sporadic avalanche-like relaxation of strain, flat temperature dependence of the phonon scattering rate) point at the presence of interacting dislocations, probably arranged into dislocation walls.

1 Introduction

We would like to dedicate this paper to the 90th birthdays of David M. Lee and John D. Reppy for their influence on physics and life in physics, and in particular—on studies of solid helium.

Mechanical properties of crystalline solids are governed by a network of linear defects—dislocations [8, 9]. The length, orientation and mobility of segments of the network determine the response of a material to an applied shear stress. These parameters can be greatly modified by impurities, cold working and thermal annealing. Hence, noninvasive techniques of characterization of the distribution of lengths and mobility of dislocations are in great demand.

Solid helium provides a special opportunity to gain further insight into the structure and dynamics of dislocation networks [10, 11]. On the one hand, it is just another solid that can be made extremely perfect and pure because only isotopic impurities remain dissolved below its solidification temperature of order 2 K, and their concentration can be controlled in a wide range. On the other, because the dynamics of helium's weakly attractive and light atoms is essentially quantum [12], dislocations are extremely mobile at low temperatures when phonon-assisted damping vanishes. Since dislocations can glide at a vanishingly low stress [13–15], sample's deformation follows a reversible elastic strain–stress relation with a renormalized shear modulus [16]—unlike dislocations in conventional solids, whose motion causes an irreversible plastic deformation.

Mobile segments of dislocations can behave as elastic strings ("fluttering dislocation") [7, 17]. The high mobility of dislocations in solid helium makes it a material of choice to investigate this phenomenon. For instance, the strong variations of the mobility of dislocations as function of temperature, impurity concentration, amplitude of shear and protocol of measurements allow for the unconventional technique of characterizing the distribution of dislocation lengths through the nonlinear nonequilibrium strain–stress response at high amplitudes of deformation to be utilized [1].

Other spectacular quantum effects are expected in solid helium; for instance, the possibility that dislocation cores might be superfluid [18]. The recently observed

mass transport through polycrystalline samples of solid ^{4}He is believed to be carried through a percolating networks of dislocations [19–24], the effect being suppressed by ^{3}He impurities at low temperatures. In this connection, it is important to know more about the distribution of dislocation lengths and their connectivity in solid ^{4}He .

In fact, the topology and dynamics of networks and tangles of linear defects in other ordered media attract considerable interest [25, 26]. While the systems in question could be as diverse as quantized vortices in superfluids and cosmic strings in the fabric of space-time, they often share similar general properties—hence, new methods of characterizing dislocation networks in solids help to further our understanding of general physics.

As an example, the linear topological defects in superfluid helium—quantized vortices—share many similarities with dislocations in solid helium [27]. Tangles of vortex lines in superfluid helium, known as quantum turbulence, have been studied since their prediction [28] and discovery in the 1950s [29]. Fairly recently the focus of research has shifted from simple random tangles to polarized structures, which are believed to dominate the dynamics of superfluid turbulence generated by velocity gradients on largest length scales [30]. This is similar to the case of plastically deformed solids, in which not individual dislocations but their correlated ensembles and long-range stress are believed to be responsible for the observed properties [31, 32]. At high temperatures, when thermally activated climb of dislocations is possible, plastic deformation creates a homogeneous random network of dislocations which can be annealed, and stresses relax via smooth visco-plastic creep. However, during a low-temperature deformation, collective interaction and multiplication of gliding dislocations was shown to result in fractal dislocation cells on all length scales and discrete slips via dislocation avalanches [32–36]. We share the attitude of Cottrell [37] that work hardening is even *harder* to understand than turbulence, which is a paradigm of complexity of driven systems [38].

The response of hcp ^{4}He , with various ^{3}He concentrations, to an AC shear stress has been investigated previously by a range of techniques at different frequencies: shear in a torsional oscillator (TO) (200 Hz–2 kHz) [39], transverse sound (1 Hz–100 kHz) [2, 16, 40–46] and ultrasound (8–50 MHz) [47–50] , scattering of thermal phonons (8–24 GHz) [4, 51–56]. Most can be explained in terms of interaction with vibrating dislocations [39, 49]. In 2004, the interest was rekindled because of the hopes [57, 58] of observing superfluidity of a bulk helium crystal (so-called supersolid). However, most experimental results of temperature and amplitude dependence of the resonant frequency and damping of a torsional oscillator containing solid helium [59–62] can currently be interpreted in terms of restraining the dislocation motion by ^{3}He impurities, whose equilibrium density near the dislocation core varies with temperature [63]: a cross-over from an underdamped to overdamped regime results in a switch, in a moderately narrow range of temperatures or amplitudes, between the "soft" and "stiff" states of solid helium [13, 64]. Experiments with oriented single crystals [13, 64] in 2010–2014 revealed a clear evidence of stiff and soft states of the same sample as a result of ^{3}He impurities interacting with dislocations and allowed to measure several properties of these interactions and to extract the distribution of node–node dislocation lengths [2].

In this paper, we report on measurements of the dynamics of dislocations in poly-crystalline hcp ^{4}He and thus infer information on the density and structure of their networks at different length scales—before and after cold working and thermal annealing. This is done through the observations of dislocations' interaction with AC shear deformation of various frequencies and amplitudes, and with ^{3}He impurities. Small-amplitude oscillations at frequencies of 161 Hz and 931 Hz allowed us to measure the temperature dependence of the shear modulus and internal friction, while medium and high amplitudes allowed to change either the number of dislocation-trapped ^{3}He atoms or the distribution of dislocation lengths, respectively. Methods of characterizing broad distributions of dislocation lengths by the equilibrium temperature dependence of the shear modulus and internal friction are introduced and suggested. We complement these by measuring the mean free path of thermal phonons (i.e., AC shear deformation at high frequencies) scattering off grain boundaries and dislocation walls through measurements of thermal conductivity in the same samples.

The paper is organized as follows. In Sect. 2, we outline the theoretical description of the dynamics of vibrating dislocations. Section 3 describes details of experimental techniques. Section 4 contains experimental results. The paper concludes with a discussion in Sect. 5 and summary.

2 Response of a Gliding Dislocation to AC Shear Stress

2.1 Dislocation Networks

Networks of gliding dislocations are made of segments terminated at either network crossings or immobile jogs. These nodes are hard to move or to get rid of due to their topological stability; cold working can increase their number while annealing at sufficiently high temperatures might remove some. Edge dislocations [15] confined to the basal plane of hcp ^{4}He along with their Burgers vector can glide virtually unimpeded at temperature $T < 1$ K [13, 44]. Isotopic impurities—^{3}He substitutions—are extremely mobile and are attracted to the rarefied regions near dislocation cores: this results in damping of dislocation motion, which is strongly temperature- and history dependent. In the high-temperature limit (when all ^{3}He impurities are free), gliding segments can be treated as strings whose motion under external forcing is damped by their interaction with the gas of phonons and ^{3}He impurities. And at low temperatures (when the trapping time of ^{3}He impurities is long), the dynamics of dislocations are affected near every trapped ^{3}He atom. However, when forced hard, a dislocation can break off a ^{3}He impurity, so at low temperature a non-equilibrium state can be maintained in which few ^{3}He impurities are trapped, thus allowing dislocations to vibrate effectively freely like in the high-temperature limit). The network of gliding dislocations has the total length per unit volume

$$\Lambda = \int_0^\infty n(L)L\mathrm{d}L, \tag{1}$$

where $n(L) = \mathrm{d}N/\mathrm{d}L$ is the distribution function of dislocation lengths L and $N(L) = \int_0^L n(L')\mathrm{d}L'$ being the number of dislocations of length smaller than L.

The distribution $n(L)$ is often parametrized by a single length scale, e.g., the average $\bar{L} = \Lambda/N(\infty)$. Then, the dimensionless scale-independent parameter $\Lambda \bar{L}^2$ characterizes the structure and anisotropy of the network (c. f., $\Lambda \bar{L}^2 = 3$ for a volume-filling simple cubic lattice, but can be much greater for a bundle of aligned dislocations [31]). Assuming the distribution of type

$$n(L) = \frac{\Lambda}{\bar{L}^2} \exp\left(-\frac{L}{\bar{L}}\right), \tag{2}$$

different experimental values of $\Lambda \bar{L}^2$ have been reported [31]: from just above 0.1–0.25 measured by the ultrasound velocity [47, 49] to above 1.0–2.5 with low-frequency torsional oscillations [39] and even above 20 in the softest ultrapure single crystals measured by ~ 10 kHz shear oscillations [65].

In principle, *fractal* self-similar dislocation networks are possible in certain cases; these could not be described by the single-scale distribution Eq. 2, and instead of a single non-dimensional structural parameter $\Lambda \bar{L}^2$ one would need to use its generalization $L^4 n(L)$ as a function of length scale L. As we will show below, our experimental technique of measuring $L^4 n(L)$ is only limited to, at best, two orders of dislocation lengths L. Hence, we would be unable to unambiguously distinguish such a multiscale distribution and will limit our analysis to the use of the model distribution Eq. 2.

2.2 Mobile Dislocations as Elastic Strings

Granato and Lücke [7] treated each gliding dislocation segment as a continuous string, hard-anchored at two points separated by a distance L along axis x. The small-amplitude transverse in-plane displacement $\xi(x, t)$ obeys the equation

$$A\ddot{\xi} + B\dot{\xi} - C\frac{\partial^2 \xi}{\partial x^2} = b\sigma_4 \cos\beta \exp(i\omega t), \tag{3}$$

where the RHS stands for the applied uniform shear stress in the basal plane σ_4 resolved in the direction of the Burgers vector $\mathbf{b}$ ($b = |\mathbf{b}|$, and β is the angle between $\mathbf{b}$ and the projection of stress on basal plane). The string is characterized [17, 66], per unit length, by its mass

$$A \approx \frac{g\rho b^2}{4\pi} \approx 3 \times 10^{-17} \, \mathrm{kg\,m^{-1}}, \tag{4}$$

energy

$$C \approx \frac{gC_{44}^{\mathrm{el}} b^2}{4\pi(1-\nu)} \approx 3 \times 10^{-12} \, \mathrm{N} \tag{5}$$

(where, for $V_m = 19.5\,\text{cm}^3\,\text{mol}^{-1}$, the density $\rho = 205\,\text{kg m}^{-3}$, interatomic distance $b = 3.58\,\text{Å}$, purely elastic constant $C_{44}^{\text{el}} = 18.6\,\text{MPa}$, Poisson's ratio $\nu = 0.3$, and factor $g \approx \ln(1/b\Lambda^{1/2}) = 9 \pm 2$), and damping parameter $B(x_3, T)$ due to ^{3}He impurities [67], phonons [68], as well as, perhaps, kinks [69, 70] and other dislocations. The fundamental frequency of the segment is then

$$\omega_0(L) = \frac{\pi}{L}\left(\frac{C}{A}\right)^{1/2} = \frac{\pi}{L}\left(\frac{C_{44}^{\text{el}}}{\rho(1-\nu)}\right)^{1/2} = \pi(1-\nu)^{-1/2}u_t L^{-1} \tag{6}$$

(where $u_t = \left(\frac{C_{44}^{\text{el}}}{\rho}\right)^{1/2} \approx 300\,\text{m s}^{-1}$ is the velocity of transverse sound), which corresponds to $f_0 = \omega_0/2\pi \sim 2\,\text{MHz}$ for $L = 100\,\mu\text{m}$ and $f_0 \sim 200\,\text{MHz}$ for $L = 1\,\mu\text{m}$.

In the low-frequency limit $\omega \ll \omega_0$, an approximate solution (neglecting term $A\ddot{\xi}$ in Eq. 3 and retaining only the first term in the Fourier series of $\xi(x)$), results in the mean amplitude [7, 72] $\bar{\xi} = L^{-1}\int_0^L \xi(x)\mathrm{d}x$:

$$\bar{\xi} \approx \frac{8bL^2}{\pi^4 C}\frac{1 - i\omega\tau}{1 + (\omega\tau)^2}\sigma_4 \cos\beta, \tag{7}$$

where the damping time $\tau(B, L)$ is

$$\tau = \frac{L^2 B}{\pi^2 C}. \tag{8}$$

Per unit volume, such a segment contributes $\bar{\xi}bL\cos\beta$ to the strain ϵ_4. Then summing the contributions of all of them, with $n(L)\mathrm{d}L$ segments with lengths between L and $L + \mathrm{d}L$ in unit volume, and using $< \cos^2\beta >= 1/2$, we obtain the dislocation contribution ϵ_4^{dis} as compared to the purely elastic contribution ϵ_4^{el} to strain,

$$\frac{\epsilon_4^{\text{dis}}}{\epsilon_4^{\text{el}}} = \alpha \int_0^\infty L^3 \frac{1 - i\omega\tau}{1 + (\omega\tau)^2}n(L)\mathrm{d}L, \tag{9}$$

with $\alpha = \frac{4b^2\sigma_4}{\pi^4\epsilon_4^{\text{el}}C} = \frac{16(1-\nu)}{\pi^3 g} \approx 0.04 \pm 0.01$. Here $\epsilon_4 = \epsilon_4^{\text{el}} + \epsilon_4^{\text{dis}}$, $\sigma_4 = C_{44}^{\text{el}}\epsilon_4^{\text{el}} = C_{44}\epsilon_4$, and hence

$$C_{44} = \frac{C_{44}^{\text{el}}}{1 + \epsilon_4^{\text{dis}}/\epsilon_4^{\text{el}}} \tag{10}$$

is the resulting elastic constant.

2.3 Response at Small Amplitudes of Strain

In equilibrium, the fraction of trapping sites near the core of a rigid dislocation, occupied by ^{3}He impurities, is $x_3 \exp(E_b/k_B T)$, where x_3 is the bulk concentration of ^{3}He and E_b is the binding energy. This makes the average distance between trapped ^{3}He atoms

$$L_i = bx_3^{-1} \exp(-E_b/k_B T). \tag{11}$$

Haziot et al. [71] found that when the dislocation velocity does not exceed $v_c \sim 45\,\mu\mathrm{m\,s^{-1}}$, trapped ^{3}He atoms are dragged by the dislocation thus contributing $B_3 \propto L_i^{-1}$ to the damping parameter B, namely [2, 67],

$$B_3 = B_0 x_3 \exp(E_b/k_B T), \tag{12}$$

where $B_0 = 0.15$ Pa s and $E_b = 0.7 \pm 0.1$ K for the concentration $x_3 \approx 3 \times 10^{-7}$ and pressure $P = 25.3$ bar. The phonon contribution to damping is [66, 68, 73] $B_{\mathrm{ph}} = \frac{\rho b^2}{8}\omega + \frac{14.4 k_B^3 T^3}{\pi^2 \hbar^2 u_D^3}$, where k_B is the Boltzmann constant, $\hbar$ is the Planck's constant, u_D is the Debye velocity. At temperature $T < 1$ K and sufficiently low frequency ω, $B_3 \gg B_{\mathrm{ph}}$, we hence assume $B \approx B_3$. We expect only a weak dependence of B_3 on pressure [74], and, in what follows, use $B_0 = 0.15$ Pa s and $E_b = 0.7$ K.

For a given dislocation length L, the cross-over from the stiff to soft state occurs around the temperature (condition $\omega\tau = 1$ in Eq. 9):

$$T_{\times}(L, f, x_3) = \frac{E_b/k_B}{\ln\left(\frac{\pi C}{2 B_0 L^3 f x_3}\right)}. \tag{13}$$

The increase of $T_{\times}$ with increasing f and x_3 was observed in experiments [2, 16].

The frequency dependence vanishes at larger strain amplitudes ϵ at which dislocation velocities $v > v_c$, so trapped ^{3}He atoms become effective anchors eventually breaking network segments of length $L > L_i(T)$ into smaller oscillating segments of average length $L_i(T)$ [1]. In this regime, the damping term $B\dot{\xi}$ in Eq. 3 should become nonlinear. The upper limit on the dislocation velocity is $v_{\max} = \frac{\pi}{2}\dot{\xi} \simeq \frac{32(1-\nu)f L^2}{\pi g b}\epsilon_4$ (from Eq. 7 with $\omega\tau = 0$, $\cos\beta = 1$ and $|y| \ll 1$). The condition for the linear response it then $\epsilon_4 < \epsilon_{c1}$ with

$$\epsilon_{c1} = \frac{\pi g b v_c}{32(1-\nu)f} L^{-2}, \tag{14}$$

which is plotted versus L by blue line in Fig. 1 for $f = 161$ Hz and $v_c = 45\,\mu\mathrm{m\,s^{-1}}$.

By plugging the distribution of dislocation lengths $n(L)$, computed with the amplitude method (see next section, Eq. 27), and the damping term Eq. 12 , Fefferman et al. [2] confirmed that it reproduces their experimental temperature dependences of the small-amplitude complex shear modulus in a single crystal of solid ^{4}He for a range of frequencies f. We would like to suggest a method of computing the length distribution $n(L)$ from $\mu(T)$ at small amplitudes. After expressing the damping time Eq. 8 through the *damping length*

$$\lambda(T) = (\omega\tau)^{-1/2} L = b\left(\frac{g C_{44}^{\mathrm{el}}}{8(1-\nu)B_0 x_3 f}\right)^{1/2} \exp\left(-\frac{E_b}{2 k_B T}\right), \tag{15}$$
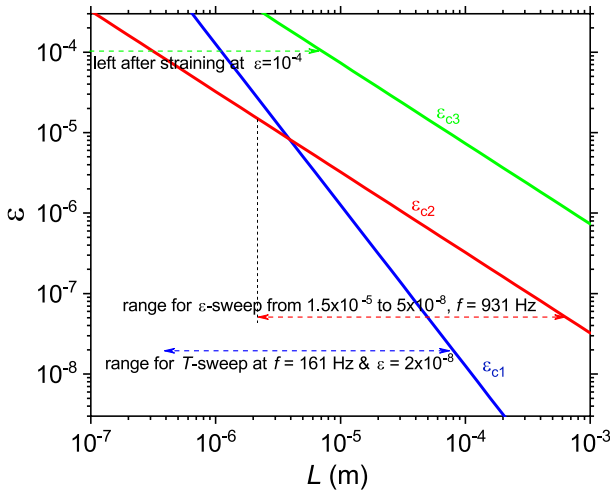
Eq. 9 becomes:

Fig. 1 Critical values of strain as function of dislocation length: ϵ_{c1} (blue line, Eq. 14), below which the equilibrium linear response holds; ϵ_{c2} (red line, Eq. 24), above which a slow ^{3}He atom does not pin a ^{3}He-free dislocation even at $T = 0$; ϵ_{c3} (green line, Eq. 28), above which dislocations stretch. Horizontal dashed lines of corresponding colors indicate ranges of L accessed by our experiments (see Sects. 4.1, 4.2 and 4.4) (Color figure online)

$$y_1 \equiv \mathrm{Re}\left(\frac{\epsilon_4^{\mathrm{dis}}}{\epsilon_4^{\mathrm{el}}}\right) = \alpha \int_0^\infty \frac{1}{1 + (\frac{L}{\lambda(T)})^4} L^4 n(L) d\ln L, \tag{16}$$

$$y_2 \equiv \mathrm{Im}\left(\frac{\epsilon_4^{\mathrm{dis}}}{\epsilon_4^{\mathrm{el}}}\right) = -\alpha \int_0^\infty \frac{(\frac{L}{\lambda(T)})^2}{1 + (\frac{L}{\lambda(T)})^4} L^4 n(L) d\ln L. \tag{17}$$

Around $L = \lambda(T)$, the fraction in RHS of Eq. 16 rapidly switches from 1 to 0, and the fraction in RHS of Eq. 17 experiences a narrow peak while being nearly zero away from it. If $L^4 n(L)$ is a slow function of $\ln(L)$, these fractions can be approximated by the Heaviside's step-function $H(1 - \frac{L}{\lambda(T)})$ and Dirac's delta-function $\Gamma\delta(\frac{L}{\lambda(T)} - 1)$ (where $\Gamma = \int_0^\infty \frac{x dx}{1+x^4} = \frac{\pi}{4} \approx 0.785$), respectively. Thus, for the case of a wide distribution $n(L)$

$$\frac{dy_1(T)}{d\ln(\lambda(T))} \approx \alpha\lambda^4 n(\lambda), \tag{18}$$

and

$$y_2(T) \approx -\alpha\Gamma\lambda^4 n(\lambda). \tag{19}$$

One can hence determine the distribution $n(L)$ experimentally from either $y_1(T)$ or $y_2(T)$, using T as a dummy parameter through $L = \lambda(T)$ from Eq. (15):

$$\lambda^4 n(\lambda) \approx \frac{2k_B T}{\alpha E_b} \frac{dy_1}{d \ln T}, \tag{20}$$

and

$$\lambda^4 n(\lambda) \approx -\frac{y_2(T)}{\alpha \Gamma}. \tag{21}$$

The switching function $(1 + (L/\lambda(T))^4)^{-1}$ has 10–90% width of $\lambda_{0.9}/\lambda_{0.1} = 3$. Hence, broad features of $n(L)$, which involve at least an order of magnitude in L, will be resolved.

The continuous description of $L_i(T)$ in Eq. 11 is only justified for $b \ll L_i(T) \ll \lambda(T)$. The LHS condition means that dislocation cores are not saturated by ^{3}He atoms at $T > T_l$. And the RHS implies that there are at least several ^{3}He atoms on segments of length $L_i(T_h) \sim \lambda(T_h)$ when $T < T_h$. Hence, the lengths L, accessible by this technique, are limited by $\lambda(T_l) < L < \lambda(T_h)$, where

$$T_l = -\frac{E_b/k_B}{-\ln x_3}, \lambda(T_l) = \left(\frac{g C_{44}^{el}}{8(1-\nu)B_0 f} \right)^{1/2} b, \tag{22}$$

here $T_l = 0.05$ K (for $x_3 = 3 \times 10^{-7}$), and $\lambda(T_l) = 0.4\,\mu$m (for $f = 161$ Hz), and

$$T_h = \frac{E_b/k_B}{-\ln(\frac{x_3 g C_{44}^{el}}{8(1-\nu)B_0 f})}, \lambda(T_h) = x_3^{-1} b, \tag{23}$$

here $T_h = 0.7$ K (for $f = 161$ Hz), and $\lambda(T_h) = 1.2$ mm (for $x_3 = 3 \times 10^{-7}$). Widening the range of frequencies f and ^{3}He concentration x_3 thus allows to broaden the range of detectable lengths L.

2.4 Hysteretic Amplitude Dependence at Moderate Strain

At higher dislocation velocities $v > v_c$ (such that bound ^{3}He atoms become effective anchors) and at stresses σ_4 sufficiently high (so the force exerted by a dislocation segment on a single slow ^{3}He impurity [1], $\sim \frac{1}{2}b\sigma_4 L$, exceeds the critical binding force [2] $F_c \sim 4E_b/b \sim 7 \times 10^{-15}$ N), the dislocation liberates itself from this anchor. In this regime, corresponding to the amplitude of shear stress exceeding $\sigma_{c2} \sim 8E_b/(b^2 L)$ and strain $\epsilon_4 > \epsilon_{c2}$ where

$$\epsilon_{c2} \sim \frac{\sigma_{c2}}{C_{44}^{el}} \sim \frac{8E_b}{b^2 C_{44}^{el}} L^{-1} \tag{24}$$

(plotted vs. L by red line in Fig. 1), the number of trapped ^{3}He impurities is no longer the equilibrium one but depends on the history.

If a sample is cooled from temperature $T \gtrsim E_b/k_B$ to $T \ll E_b/k_B$ while at an oscillatory strain of a moderate amplitude $\epsilon_4 > \epsilon_{c2}$, a non-equilibrium configuration with no trapped ^{3}He atoms can be sustained. Then, by gradually reducing the amplitude

at low temperature, one can observe a gradual stiffening of the crystal as dislocation segments of progressively longer lengths L become immobilized by avalanche-like swamping of their cores by ^{3}He atoms. Following Granato and Lücke [1, 7], one can formally split all segments into those with $L < L_c(\sigma_4)$ which are sessile (strongly pinned by multiple ^{3}He impurities), and those with $L > L_c(\sigma_4)$ which are glissile with $B_3 \approx 0$ (free from any ^{3}He impurities), where

$$L_c \approx \frac{2F_c}{b\sigma_4} \sim \frac{8E_b}{b^2 C_{44}^{el}} \epsilon_4^{-1}. \tag{25}$$

Then, Eq. 9 becomes

$$y_1 \equiv \mathrm{Re}\left(\frac{\epsilon_4^{dis}}{\epsilon_4^{el}}\right) \approx \alpha \int_{L_c(\epsilon)}^{\infty} L^4 n(L) d\ln L. \tag{26}$$

There is no dissipation from ^{3}He impurities in this simple model, hence, $y_2 \equiv \mathrm{Im}\left(\frac{\epsilon_4^{dis}}{\epsilon_4^{el}}\right) \approx 0$.

Thus, from the changes in the dislocation contribution ϵ_4^{dis} to total strain ϵ_4 while reducing ϵ_4, $n(L)$ can be determined (using $L = L_c(\epsilon_4)$ from Eq. 25):

$$L_c^4 n(L_c) \approx -\alpha^{-1}\frac{dy_1}{d\ln L_c} = -\alpha^{-1}\frac{dy_1}{d\ln \epsilon_4}, \tag{27}$$

where we assumed $\epsilon_4 \propto \sigma_4$ neglecting the dependence of ϵ_4/σ_4 on y_1. This noninvasive method allows to characterize the distribution of dislocation lengths as was done for polycrystals [1, 50, 82] and single crystals [2]. As far as we are aware, it was so far only possible to apply it to solid helium—thanks to the short relaxation time of ^{3}He impurities [48] and high mobility of dislocations.

In a polycrystal, at the same applied macroscopic strain ϵ, differently oriented grains are subject to different resolved stress in the basal plane ϵ_4. Hence, the resolution of the method in terms of L_c becomes broadened. Furthermore, with our method of twisting a rod of solid helium, only the outer part of the rod contributes to the torque effectively. However, as was discussed in the preceding section, sufficiently broad features of the distribution $n(L)$ can still be observed.

2.5 Work hardening at large strain

Finally, at large stress when the force on a dislocation $\sim bL\sigma_4$ becomes comparable with its tension C, the linear Eq. 3 no longer holds and, above the yield stress σ_{c3} and strain ϵ_{c3}, an irreversible plastic deformation takes place: dislocations stretch, cross and multiply, thus creating new nodes and jogs which result in a stiffer crystal. Subsequent annealing at higher temperature would normally remove some of the consequences of cold working. The microscopic processes of work hardening are complex and are yet poorly understood, so we will resort to the following naive model. When the force exerted on a dislocation of the initial

length L, $F \sim b\sigma_4 L$, exceeds the tension from both ends, $2C$, the dislocation will keep stretching until it either multiplies by the Frank–Read mechanism or crosses with another one and forms a new node. All dislocations longer than L_{max}, for which the yield stress

$$\epsilon_{c3} = \frac{\sigma_{c3}}{C_{44}^{el}} \sim \frac{2C}{bC_{44}^{el}} L_{max}^{-1} \tag{28}$$

(plotted vs. L by green line in Fig. 1) is smaller than tEpsilonc3he applied ϵ_4, will be modified by this mechanism. Accordingly, if annealed samples had dislocations of length up to $L_{max} \sim 0.1$ mm, straining with amplitude $\epsilon_4 \gtrsim 10^{-5}$ will change the distribution $n(L)$ by reducing the long-length cut-off L_{max} and populating shorter length scales. Repetitive straining up to amplitude ϵ should thus eliminate all dislocations of lengths $L > L_{max} \sim \frac{2C}{bC_{44}^{el}} \epsilon_4^{-1}$, and the sample will be held on the verge of yielding in a critical state with small additional dissipation (due to either nonlinearity of stretching dislocations or fast elimination of some of the freshly made crossings).

In reality, the dynamic response of a dislocation network could be even more complicated: for instance, continuous AC-straining might generate not a homogeneous network of gliding dislocations but fractal dislocation cells (where dislocations are concentrated within fuzzy walls) each rotating as a whole in response to shear deformation. One might expect that a subsequent reduction of the strain amplitude, at low temperature, would not affect the structure of the achieved dislocation network; however, we found evidences that this is not quite true (see Sect. 4.4).

Equations 24 and 28 give the limit on the range of dislocation lengths L that can be explored using the amplitude technique Eq. 27 described in the previous section. Namely, in order to avoid the stretching of the longest dislocations of length L_{max}, strain should not exceed Eq. 28. Hence, through Eq. 24 the shortest accessible lengths L_{min} are such that

$$\frac{L_{max}}{L_{min}} \sim \frac{bC}{4E_b} \approx 30. \tag{29}$$

The actual value of this range depends on the numerical prefactors in Eqs. 24 and 28, which are unknown; we can only conclude that the accessible range of dislocation lengths covers 1–2 orders of magnitude.

2.6 Effective Shear Modulus of a Polycrystal

There exist two simplified methods of calculating the effective shear modulus μ of an isotropic polycrystal at length scales larger than grain sizes: either while assuming a uniform stress (Voigt [75]),

$$\mu_V = C_V + \frac{2}{5} C_{44}, \tag{30}$$

where

$$C_V = \frac{1}{30}(7C_{11} - 5C_{12} - 4C_{13} + 2C_{33}),$$

or while assuming uniform strain (Reuss [76]),

$$\mu_R = \left(C_R^{-1} + \frac{2}{5}C_{44}^{-1} \right)^{-1}, \tag{31}$$

where

$$C_R = 15 \left(\frac{4(C_{11} + C_{12}) + 8C_{13} + 2C_{33}}{C_{33}(C_{11} + C_{12}) - 2C_{13}^2} + \frac{6}{C_{66}} \right)^{-1}.$$

As was shown by Hill [77], neither can be realistic; hence a compromise, often in the form of their arithmetic mean, was found to be close to reality [78]. We assume that dislocation motion only softens one elastic constant (making it complex), $C_{44}(\epsilon_4^{dis}/\epsilon_4^{el})$. We hence used Hill's formula

$$\mu = \frac{1}{2} \left[\mu_V(C_{44}) + \mu_R(C_{44}) \right] \tag{32}$$

along with the experimental values of μ to solve for complex C_{44} Eq. 10, and hence for $\epsilon_4^{dis}/\epsilon_4^{el}$.

Greywall [79] found that the elastic constants C_{ij} for hcp ^{4}He at molar volume V_m scale as $C_{ij} = \mathcal{P}(V_m)c_{ij}$, where $\mathcal{P} = (V_0/V_m)^{5.73}$, and c_{ij} at $V_0 = 20.97\,\mathrm{cm}^3\,\mathrm{mol}^{-1}$ and $T \sim 1$ K were measured by David Lee and coworkers [80]: $c_{11} = 40.5$ MPa, $c_{12} = 21.3$ MPa, $c_{13} = 10.5$ MPa, $c_{33} = 55.4$ MPa, $c_{44}^{el} = 12.4$ MPa, and $c_{66} = \frac{1}{2}(c_{11} - c_{12}) = 9.6$ MPa. For our hcp ^{4}He at $V_m = 19.5\,\mathrm{cm}^3\,\mathrm{mol}^{-1}$ ($\rho = 205$ kg m^{-3}, $p_m = 53$ bar, $T_m = 2.4$ K [81], $\Theta_D = 31.6 \pm 0.2$ K), $\mathcal{P} = 1.50$, $C_V = 12.32$ MPa, $C_R = 29.55$ MPa, and we did not adjust the values of C_{ij} to account for temperatures of our experiment $T \sim 0.1$ K.

In principle, $C_{44}(\epsilon_4^{dis}/\epsilon_4^{el})$ can take any values between $C_{44} = C_{44}^{el} = \mathcal{P}c_{44}^{el} = 18.6$ MPa when dislocations are immobilized (then $\mu(0) \equiv \mu_0 = 18.9$ MPa, as in a stiff crystal at $T = 0$) and $C_{44} = 0$ when there are many parallel mobile dislocations, so the low limit for a soft crystal becomes $\mu = 6.2\,\mathrm{MPa} = 0.33\mu_0$. However, for realistic networks the low limit on C_{44} (and hence on μ) for the soft state is set by the value of $L^4 n(L)$ through Eq. 16. For instance, with the distribution of type Eq. 2,

$$y_1 = 6\alpha\Lambda\overline{L}^2, \tag{33}$$

which for an isotropic distribution with $\Lambda\overline{L}^2 = 3$ gives $y_1 \approx 0.7$ (and hence from Eq. 32, $\mu/\mu_0 \approx 0.8$), independent of $\overline{L}$. In our experiments, quite similar values of the lowest μ/μ_0 at $T \gtrsim 0.3$ K were found: ~ 0.65 for as-grown samples and ~ 0.73 for annealed ones.

2.7 Interaction of Thermal Phonons with Dislocations

The thermal conductivity of solid helium is dominated by the contribution from transverse phonons of frequency [83] $\omega_{ph}(T) \sim 3.8 k_B T/\hbar$. For temperature $T = 0.1$ K (0.3 K), these correspond to $f_{ph}(T) = 3.8\frac{k_B T}{h} = 8$ GHz (24 GHz). The interaction of phonons with defects is characterized by the mean free path $\ell = u_t \tau_{ph}$ (where τ_{ph} is the relaxation time). Usually, the resonant scattering (absorption and re-emission) of phonons by fluttering dislocations [17] is the dominant process. If the typical size of dislocations $L \sim \Lambda^{-1/2}$ is so small that their $\omega_0(L) \sim \omega_{ph}$, i.e., $L = 20$ nm (7 nm) for $T = 0.1$ K (0.3 K), then [17]

$$\ell \sim \frac{\omega_0}{\Lambda u_t} \sim \frac{1}{\Lambda L} \sim L, \tag{34}$$

while for longer segments it rapidly increases with L,

$$\ell \sim \frac{\omega_{ph}}{\Lambda u_t} \sim \frac{L^2}{b} \frac{T}{\Theta_D}. \tag{35}$$

The scattering off the static strain field of randomly oriented dislocations [84, 85] is always weaker (and has an opposite temperature dependence):

$$\ell \sim \frac{3 \times 10^{-2} u_t}{\gamma^2 b^2 \Lambda \omega_{ph}(T)} \sim \frac{L^2}{b} \frac{\Theta_D}{T}, \tag{36}$$

where $\gamma = 2.7$ is the Grünisen parameter [79].

And with the static strain field of grain boundaries [84, 85] with a large tilting angle $\alpha_{GB} \sim 1$, one can expect a nearly temperature-independent rate of scattering, giving the phonon m.f.p. of order the size of grains ξ:

$$\ell \sim 30\gamma^{-2}\alpha_{GB}^{-2}\xi \approx 4\alpha_{GB}^{-2}\xi. \tag{37}$$

The case of scattering off the static strain of dislocation walls is probably intermediate between the last two.

The thermal conductivity of polycrystalline samples of hcp ^{4}He was measured down to $T = 30$ mK by Armstrong et al. [4]. For molar volumes 20.2–21.0 cm^3 mol^{-1} up to $T = 0.5$ K, the inferred phonon mean free path $\ell(T)$ was found to be either temperature independent or weakly decreasing with increasing T, which was interpreted as the scattering off grain boundaries and strain field of edge dislocations.
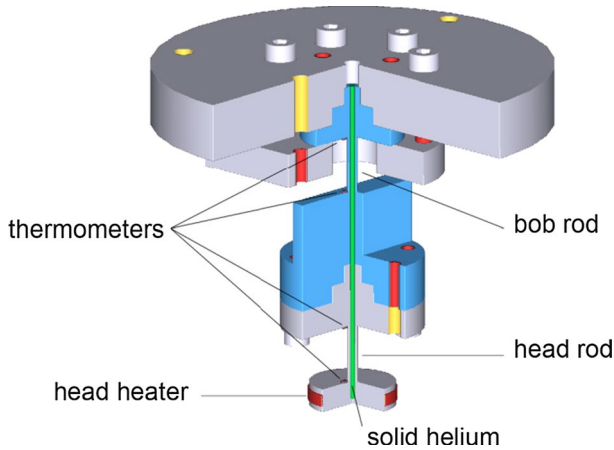
Fig. 2 Experimental cell. Solid helium is shown by green color; the studied regions ('head rod' and 'bob rod') are between two pairs of thermometers near either end (Color figure online)

3 Experimental Techniques

3.1 Experimental Cell

The design of the experimental cell, shown in Fig. 2, was similar to that of coupled TO (with the torsional head and bob, and two torsion rods), developed by John Reppy and coworkers [86] to study liquid and solid helium, but with one important difference: there was no helium inside the torsional head. All solid helium under study was located inside two cylindrical axial channels [87], both of length $z = 10.1$ mm and inner diameter $d = 1.1$ mm, made through the torsion rods of outer diameter $D = 1.9$ mm. In other words, two different samples of solid helium inside this channel could be investigated: one ('head rod') between the head and bob, and the other ('bob rod') between the bob and heavy platform (shown at the top in Fig. 2) which was rigidly attached to the dilution refrigerator. Using the capacitive coupling between flat electrodes on the bob and platform, one could drive and detect AC rotation of the bob. Two high-Q oscillatory modes thus allowed to twist the rods and to monitor small changes of the corresponding resonant frequencies f_r and bandwidths $f_b = Q^{-1}f_r$ (which reflect the change in the shear modulus and internal friction of twisted solid helium) of the TOs. The thermal conductivity of both rods of solid helium could be measured with four calibrated RuO_2 thick-film resistor thermometers glued with varnish at each end of both rods and a resistive heater in the torsion head.

Samples of solid helium were grown by the blocked-capillary technique out of commercial ⁴He with the ³He concentration $x_3 \sim 3 \times 10^{-7}$. The cell was initially filled with liquid helium at pressure 84 bar, after which the temperature of the platform was gradually lowered through the corresponding melting temperature $T_m(84 \, \text{bar}) = 3.1$ K—thus freezing a plug in the filling capillary. After that, the fixed trapped amount of helium of mean molar volume $V_m = 19.5 \, \text{cm}^3 \, \text{mol}^{-1}$ and

density $\rho = 205$ kg m^{-3} (final melting temperature and pressure $T_m = 2.4$ K and $P_m = 53$ bar) solidified in the given volume from the cold end at the platform toward the dead end in the head. During the growth of the sample and associated relaxation of pressure gradients as the density of growing solid decreased by 6%, solid helium experiences viscous-like flow along the rod, which should have resulted in multiple grains and dislocations in addition to those created during solidification.

3.2 Torsional Oscillator

Our aim was to determine the relative contribution of gliding dislocations to strain (i.e., the complex $\epsilon_4^{dis}/\epsilon_4^{el}$ in Eq. 9) when subject to an AC shear at a low frequency $f \ll f_0$, Eq. 6. This was done via measurements of the rigidity and losses of a rod of solid ^{4}He when subject to torsional oscillations. Due to the relatively small diameter of the channel and low density of helium, the effect of helium's inertia on the TO frequency was negligible.

The cell comprises two torsional oscillators in series, each having a metal head of a constant moment of inertia I_i and a hollow metal stem containing a sample of solid ^{4}He —whose complex rigidity is $K_i = K_{BC,i} + K_{He,i}$ ($i = 1$ for bob, 2 for head rod). Here $\text{Re}(K_{BC,i}) = \frac{\pi d^4}{32z}(D^4/d^4 - 1)\mu_{BC}$ (with $\mu_{BC} \approx 52$ GPa being the low-temperature shear modulus of BeCu) is the rigidity of the metal stem, and $\text{Im}(K_{BC,i})$ represents losses in the stem including the electronic feedback (Q-spoiler) which was sometimes added in order to reduce the ringing time of the TO. In conventional notations, $\text{Im}(K_i) = \gamma_i \omega_i$, where the dissipative torques are $-\gamma_i \dot{\theta}_i$ while θ_i are the twisting angles of rods. $K_{He,i} = \frac{\pi d^4}{32z}\mu_i$, where the complex $\mu_i(C_{44}(\epsilon_4^{dis}/\epsilon_4^{el}))$ represents both the shear modulus and internal friction of polycrystalline solid helium. The system, described by equations

$$\begin{cases} I_1\ddot{\theta}_1 = -K_1\theta_1 + K_2\theta_2 + \mathcal{T} \\ I_2(\ddot{\theta}_1 + \ddot{\theta}_2) = -K_2\theta_2, \end{cases} \tag{38}$$

has two normal modes of (thanks to $I_1/I_2 = 8.0 \gg 1$ and $\text{Re}(K_1) \approx \text{Re}(K_2) = K$) well-separated frequencies $f_{r,i} \approx \frac{1}{2\pi}\left(\frac{K}{I_i}\right)^{1/2}$ and bandwidths $f_{b,i} \approx \frac{1}{2\pi}\frac{\gamma_i}{I_i}$ (namely, the symmetric mode with frequency $f_{r1} = 161$ Hz and quality factor $Q_1 = 4 \times 10^5$, and the antisymmetric one with $f_{r2} = 931$ Hz and $Q_2 = 4 \times 10^6$).

The oscillators were driven by the torque applied to the bob $\mathcal{T}(t) \propto V_{in}$, with AC voltage $V_{in} \propto \exp(i\omega t)$ of frequency $\omega \approx 2\pi f_{r,i}$, while the angle of twist of the bob rod $\theta_1(t) = \Theta_1 \exp(i\omega t)$ was detected. The complex response $\Theta_1(\omega)$ was of the Lorentzian shape; hence, the following quantities could be monitored [88]: f_r, f_b, Θ_1. The values of f_r and f_b (unless necessary, we will omit the index i in $f_{r,i}$, $f_{b,i}$ and μ_i) are related to the effective complex shear modulus as

$$\mu = \mu_0\left(\frac{f_r - f_{r,\text{empty}}}{f_{r,0} - f_{r,\text{empty}}} + i\frac{f_b - f_{b,\text{empty}}}{2(f_{r,0} - f_{r,\text{empty}})}\right), \tag{39}$$

where μ_0 and $f_{r,0}$ correspond to the stiff limit with immobile dislocations (say, at $T = 0$ when $\epsilon_4^{\text{dis}} = 0$), and $f_{r,\text{empty}}$ and $f_{b,\text{empty}}$ are the resonant frequency and bandwidth of an empty oscillator. From this (see next Section), one can extract the complex ratio of the dislocation-induced strain to the purely elastic strain, $\epsilon_4^{\text{dis}}/\epsilon_4^{\text{el}} \equiv y_1 + i y_2$ as a measure of the dislocation-induced softening [89].

The amplitude of strain at the rim of the bob rod is then $\epsilon = \frac{d}{2z}\Theta_1$ when in the symmetric mode at $f_{r1} = 161$ Hz, and at the rim of the head rod $\epsilon = \frac{d}{2z}\Theta_2 = \frac{d}{2z}\left(\frac{f_{r2}}{f_{r1}}\right)^2 \Theta_1$ when in the antisymmetric mode at $f_{r2} = 931$ Hz (because the twisting angle of the head rod is $\Theta_2 = \frac{I_1}{I_2}\Theta_1 = \frac{f_{r2}^2}{f_{r1}^2}\Theta_1$). The amplitude Θ_1 is related to the current I, detected by the current–voltage converter, through

$$\Theta_1 = \frac{d_{\text{gap}}}{r_{\text{arm}}}\frac{I}{\omega c U_0} = \frac{d_{\text{gap}}^2 I}{2\pi\epsilon_0 r_{\text{arm}} A f U_0} \tag{40}$$

(here the gap is $d_{\text{gap}} = 0.3 \pm 0.1$ mm, arm $r_{\text{arm}} \approx 6 \pm 1$ mm, capacitance $c = \frac{\epsilon_0 A}{d_{\text{gap}}}$ with the electrode area $A \approx 1$ cm^2, dc bias voltage $U_0 = 290$ V).

3.3 Thermal Conductivity

To detect dislocations, one can measure the thermal conductivity κ at temperatures below ~ 0.5 K, at which phonon–phonon interactions are infrequent so the mean free path (m.f.p.) ℓ of thermal phonons is controlled by scatterings off either sample boundaries or crystal defects. The power $\dot{Q}$ (typically within 10 nW–1 μW range) was applied in the head heater; this resulted in the temperature difference ΔT (typically between 0.1 and 1 mK), proportional to $\dot{Q}$, between two thermometers at both ends of rods, distance z apart. The value of

$$\kappa_{\text{total}} = \frac{4z}{\pi d^2}\frac{\dot{Q}}{\Delta T} \tag{41}$$

was thus calculated. While thermal conductivity of hcp ^{4}He is known to be strongly anisotropic, we assume that our polycrystal samples had grain size of order $\lesssim d$— hence, within the distance between the thermometers, $z = 10.1$ mm, the heat flux passes through several randomly oriented grains, and the anisotropy is mainly averaged out. The thermal conductivity of the empty cell, κ_{cell}, did not exceed 20% of the total thermal conductivity $kappa_{\text{total}}$ at the lowest temperatures; it agreed with our estimates for the BeCu walls and was subtracted: $\kappa(T) = \kappa_{\text{total}}(T) - \kappa_{\text{cell}}(T)$.

The kinetic theory formula for thermal conductivity [90] of solid helium,

$$\kappa = \frac{1}{3}C_{\text{v}}\bar{u}^2\tau_{\text{ph}} = \frac{1}{3}C_{\text{v}}\bar{u}\ell, \tag{42}$$

where (for $\Theta_D = 31.6$ K at $V_m = 19.5$ cm^{3}m^{-1}) $C_{\text{v}} = \frac{12\pi^4 N_A k_B}{5}\left(\frac{T}{\Theta_D}\right)^3 = 3.18 \times 10^3 T^3$ J K^{-4} m^{-3} is the phonon specific heat and $\bar{u} = \frac{\langle u^{-2}\rangle}{\langle u^{-3}\rangle}$ is the phonon velocity averaged for all branches and crystal orientations

(which we approximate by the Debye velocity, $u_D = \frac{k_B \Theta_D}{2\pi\hbar}\left(\frac{4\pi V_m}{3N_A}\right)^{1/3} = 337$ m s^{-1}), allows to determine the relaxation time τ_{ph} and m.f.p. $\ell = \bar{u}\tau_{ph}$. As the contribution from longitudinal phonons is small ($\sim 13\%$), the obtained m.f.p. is mainly due to transverse phonons.

In the presence of additional defects characterized by their own τ_{def}, the reduced value of τ_{ph}—from τ_0 in an annealed sample—can be expressed through the increased rate of scattering, $\tau_{ph}^{-1} = \tau_0^{-1} + \tau_{def}^{-1}$. One can thus calculate ℓ_{def} due to this additional scattering mechanism using

$$\ell_{def}^{-1} = \ell^{-1} - \ell_0^{-1}. \tag{43}$$

4 Experimental Results

We investigated the following types of samples:

(i) *As-grown* They are expected to be quite inhomogeneous with dislocations and grain boundaries left after crystallization as well as due to the plastic flow caused by the pressure gradients during solidification at continuously decreasing temperature from 3.1 K to 2.4 K and pressure from 84 bar to 53 bar, and subsequent cooling.

(ii) *Annealed* at $T = 1.8$ K. This was usually done overnight and resulted in the removal of the effect of many initial defects as seen by our measurements. Further annealing at 2.0 K did not change any of the observed properties.

(iii) *Cold-worked* by large-amplitude ($\epsilon \sim 10^{-4}$, $\dot{\epsilon} \sim 1$ s^{-1}) AC twisting at $T = 0.3$ K for about 15 hours. Only the head rod at the high-frequency antisymmetric mode could be driven at the required amplitude of twist $\epsilon \gtrsim 10^{-4}$.

(iv) *Hardened* by stopping the large-amplitude twisting at low temperature $T = 0.03$ K. This caused an effective arrest of the majority of mobile dislocation segments, which could only be lifted by annealing above 0.5 K.

(v) *Recovered* after cold-working. It was found that 1 hour of annealing at $T = 1.0$ K almost completely removes the hardening effects of cold working (i.e., restores the state (ii)). However, an overnight annealing at 0.55–0.7 K resulted in only a partial recovery—this allowed to look into the dynamics of recovery from the *hardened* state.

4.1 Torsional Oscillator: Equilibrium Temperature Dependence at Small Strain

In Fig. 3, we show examples of the equilibrium temperature dependences of the relative changes of the real and imaginary parts of the shear modulus μ/μ_0. They are computed, using Eq. 39, from $f_r(T)$ and $f_b(T)$ measured at small drive amplitude in a sample inside the head rod (at frequency $f_r \approx 931$ Hz and strain $\epsilon < 5 \times 10^{-7}$) before and after annealing, as well as in a sample inside the bob rod (at $f_r \approx 161$ Hz and strain $\epsilon < 2 \times 10^{-8}$) before annealing. And in Fig. 4, $\mathrm{Re}(\mu/\mu_0)$ and $\mathrm{Im}(\mu/\mu_0)$ are converted into $\mathrm{Re}(\epsilon_{dis}/\epsilon_{el})$ and $\mathrm{Im}(\epsilon_{dis}/\epsilon_{el})$ using Eq. 32. The effect of softening at high temperatures due to ^{3}He un-trapping, in

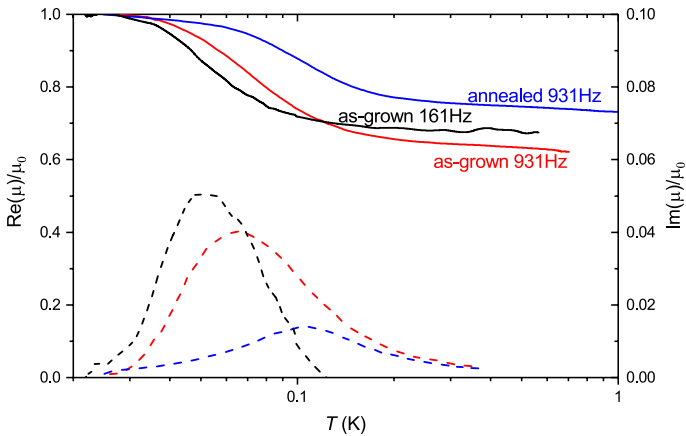**Fig. 3** Temperature dependence of the normalized shifts of the resonance frequency $(f_r(T) - f_{r,0})/(f_{r,0} - f_{r,empty}) = Re(\mu/\mu_0)$ (solid lines, left axis) and bandwidth $(f_b(T) - f_{b,empty})/2(f_{r,0} - f_{r,empty}) = Im(\mu/\mu_0)$ (dashed lines, right axis—note a tenfold difference in vertical scales) (Color figure online)
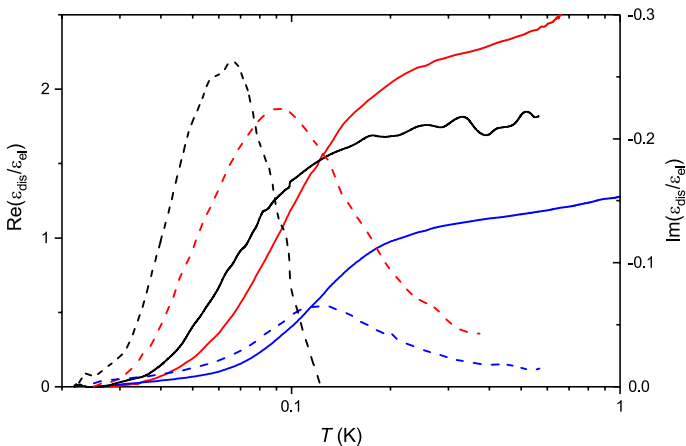

Fig. 4 Temperature dependence of the ratio of the dislocation-assisted strain ϵ_{dis} to that due to the elastic deformation ϵ_{el} (real part shown by solid lines, left axis; imaginary part shown by dashed lines, right axis), obtained from the data in Fig. 3. Legend as in Fig. 3 (Color figure online)

both $f_r(T)$ and $f_b(T)$, is evident in all samples. The cross-over temperature $T_\times$ of as-grown samples is larger for larger driving frequency, in agreement with Eq. 13. One can see that annealing results in the reduction of both the magnitude of high-temperature softening and of the associated dissipation peak.
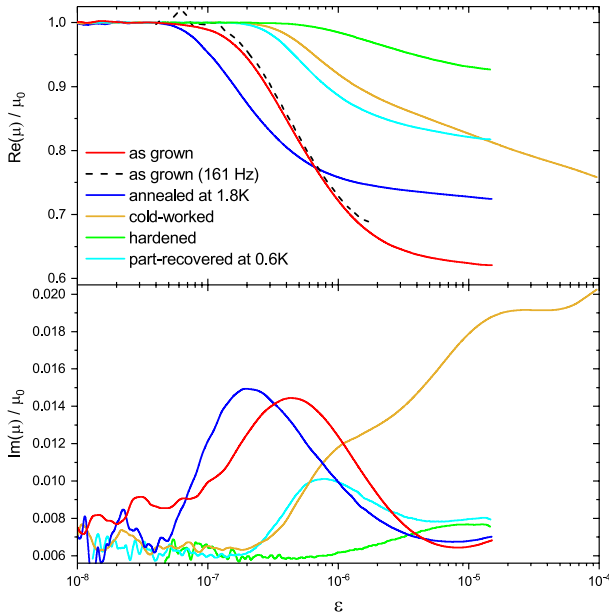
Fig. 5 Amplitude dependence of the shear modulus $\mu(\epsilon)$ (Eq. 39) measured at $T = 0.03$ K while decreasing the strain ϵ. Solid lines are for the head rod (antisymmetric mode near $f_r = 931$ Hz), the black dashed line corresponds to an as-grown sample in the bob road driven at the symmetric mode near $f_r = 161$ Hz. Bottom panel: $\text{Im}(\mu)/\mu_0$ versus ϵ. In order to speed-up the relaxation of the TO to the changing $f_r(\epsilon)$ and $f_b(\epsilon)$, some electronic feedback in the detect-drive circuit (effective damping) was added, which caused the upward shift of the base line by ~ 0.006 (Color figure online)

4.2 Torsional Oscillator: Amplitude Dependence at Moderate Strain

Most samples were initially cooled from $T \sim 0.3$ K to 0.02–0.03 K while being driven at a moderate strain amplitude of $\epsilon \sim 2 \times 10^{-6}$ for the bob-rod samples studied at $f_r = 161$ Hz and $\epsilon = 1.5 \times 10^{-5}$ for the head-rod samples studied at $f_r = 931$ Hz. Then changes in $f_r(\epsilon)$ were monitored while slowly decreasing ϵ in small steps. To speed up the relaxation of TO to the evolving resonance frequency, additional electronic damping was introduced in order to reduce the quality factor Q. In Fig. 5, we show examples of the real and imaginary parts of the shear modulus measured at temperature $T \sim 0.03$ K while reducing the strain amplitude ϵ. With decreasing ϵ from $\sim 10^{-5}$ to 10^{-7}, the increase of $\text{Re}(\mu)$ toward its low-temperature stiff limit μ_0 is interpreted as an arrest of progressively longer segments by ^{3}He atoms. This is always accompanied by an increased $\text{Im}(\mu)$; this dissipation is likely due the interaction between ^{3}He atoms and dislocation segments slightly shorter than the critical length, Eq. 25. And in samples, cold-worked by higher strains $\epsilon \sim 10^{-4}$, the substantial enhancement in $\text{Im}(\mu)$ at ϵ between $\sim 10^{-4}$ to 10^{-6} is most likely due to the losses during the plastic response with its nonlinear and hysteretic stress–strain loop.

One can see close agreement of $\text{Re}(\mu)$ versus ϵ for as-grown samples in the head and bob roads, which are measured at very different frequencies, 931 Hz and 161 Hz—similar to reported in [2]. With a reservation that these are two different
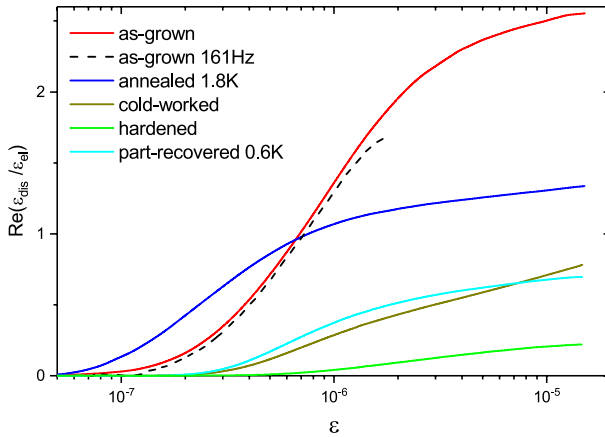
Fig. 6 The ratio of the dislocation-assisted strain ϵ_{dis} to that due to the elastic deformation ϵ_{el} measured at $T = 0.03$ K while decreasing the strain ϵ. Legend as in Fig. 5 (Color figure online)

samples, we take this as an argument in favor of the consistency of the technique of characterizing dislocations by the amplitude dependence of shear modulus measured at different frequencies. The amplitude dependences of $\mathrm{Re}(\epsilon_{dis}/\epsilon_{el})$, calculated from $\mathrm{Re}(\mu)/\mu_0(\epsilon)$ using Eq. 32. are shown in Fig. 6. For the sample, cold-worked at high strain of $\epsilon \sim 10^{-4}$, we only show data in the same range of moderate $\epsilon < 1.5 \times 10^{-5}$ beyond which the nonlinear response of stretching dislocations would deem further analysis misleading.
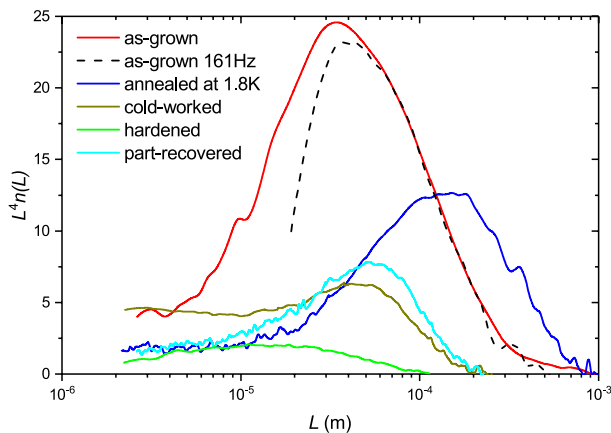

Fig. 7 $L^4 n(L)$, obtained from the data in Fig. 6 using Eq. 27, versus the network length L calculated with Eq. 25. Legend as in Fig. 5 (Color figure online)

4.3 Analyses in Terms of Dislocation Length Distribution

In Fig. 7, $L^4 n(L)$, obtained from the curves in Fig. 6 using Eq. 27, are plotted versus the network length $L(\epsilon)$ calculated with Eq. 25. As the high-frequency mode allowed a wider range of strain amplitude as well as a better signal-to-noise ratio, only this mode was used for further systematic investigations. All curves demonstrate a bell-shaped peak, which is usually accompanied, at shorter lengths L, by a "plateau". The model distribution (Eq. 2) does predict an asymmetric peak of form

$$L^4 n(L) = \Lambda \overline{L}^2 \left(\frac{L}{\overline{L}}\right)^4 \exp\left(-\frac{L}{\overline{L}}\right) \tag{44}$$

of height $\left(\frac{4}{e}\right)^4 \Lambda \overline{L}^2 = 4.7 \Lambda \overline{L}^2$ at $L_{\text{peak}} = 4\overline{L}$ and ratio $L_2/L_1 = 3.3$ (where L_1 and L_2 are the effective cut-offs at the 50% level of $\xi(L)$ such that $L_1^4 n(L_1) = L_2^4 n(L_2) = \frac{1}{2}\left(\frac{4}{e}\right)^4 \Lambda \overline{L}^2$). However, experimental peaks $L^4 n(L)$ versus $\ln L$ turned out to be more symmetric than the skewed (Eq. 44), and the ratio $L_2/L_1 \approx 10$ for all samples (subject to some limitations on the definition of L_1 due to the presence of the short-scale plateau, see below)—always greater than the model's $L_2/L_1 = 3.3$. This hints at inhomogeneous broadening, and there might be several genuine reasons for this. Firstly, the realistic distribution might differ from the simple form (Eq. 2). Secondly, the method [1, 7] (Eqs. 25–26), in which all dislocations are divided into either completely immobilized or completely free, is overly simplified as it does not account for any cross-over between these extreme cases. Thirdly, some inevitable broadening should arise from the radial inhomogeneity of strain [89]. Finally, the samples most probably contained many grains of different orientation.

The appearance of plateaus at shortest lengths is likely an artifact of ensuing yield at high amplitudes of strain. Indeed, in Sect. 2.5, from Eq. 29 we found that the technique could only represent the range of dislocation lengths within about factor of 30 (or perhaps two orders of magnitude at best). It is interesting to see that plateaus in Fig. 7 do appear at lengths of order 1/30 of the large-scale effective cut-off L_2, specific for each sample. As the plateaus appear at short lengths L corresponding to the strain $\epsilon = \epsilon_{c2}(L) \sim 10^{-6}$–$10^{-5}$, they are likely due to the nonlinear plastic response of stretching and multiplying the longest dislocations of length L such that $\epsilon = \epsilon_{c3}(L)$. This is supported by the fact that such a plateau is the most prominent for the sample which was cold-worked beginning from much larger values of strain $\epsilon \sim 10^{-4}$. The plateaus do appear at the same range of strain $\epsilon \gtrsim 3 \times 10^{-6}$, at which an additional dissipation kicks in (Fig. 5, bottom panel)—which we attribute to the nonlinear plastic response of dislocations. With hindsight, in order not to modify the dislocation network by excessive strain while measuring $L^4 n(L)$ by the amplitude method, we should have better used a narrower range (like $\epsilon < 2 \times 10^{-6}$ as we did for $f = 161$ Hz scans, and not $\epsilon < 1.5 \times 10^{-5}$)—as it seems amplitudes $\epsilon \gtrsim 3 \times 10^{-6}$ already cause some stretching of the longest dislocations (although, fortunately, not their removal—as the long-length sides of $L^4 n(L)$, measured at both frequencies, are identical for *as-grown* samples, shown in Fig. 7).

Table 1 Parametrization of the dislocation network in terms of the peak value $L^4n(L)_{\text{peak}}$ and position L_{peak} for the five samples from Fig. 7, investigated at $f_r = 931\,\text{Hz}$

Sample	$L^4n(L)_{\text{peak}}$	L_{peak} (µm)	$\Lambda\bar{L}^2$	$\bar{L}$(µm)	Λ(cm^{-2})
As-grown	24.6	34	15.7	8.5	2.2×10^7
Annealed	12.6	140	8.1	35	6.6×10^5
Cold-worked	6.3	46	4.0	11.5	3.0×10^6
Hardened	2.0	12	1.3	3.0	1.4×10^7
Part.-recovered	7.8	54	5.0	13.5	2.7×10^6

An alternative explanation for the appearance of plateaus in $L^4n(L)$ could be the existence of multi-scale distributions of dislocation lengths due to self-similar dislocation structures down to much shorter lengths—as observed in certain circumstances [32]. However, because of the limitations of our technique, we cannot test this hypothesis.

The magnitude and position of peaks, $L^4n(L)_{\text{peak}}$ and L_{peak}, for the five samples from Fig. 7, investigated at $f_r = 931\,\text{Hz}$ are shown in Table 1 along with the inferred parameters, characterizing the network of gliding dislocations: $\Lambda\bar{L}^2 = 3 \times L^4n(L)_{\text{peak}}/4.7 = 0.64 \times L^4n(L)_{\text{peak}}$ (the factor 3 comes thanks to the approximately threefold broadening of the peaks of $L^4n(L)$ versus $\ln L$), $\bar{L} = L_{\text{peak}}/4$ and $\Lambda = \Lambda\bar{L}^2/\bar{L}^2$.

The *as-grown* sample has the highest of all value of $\Lambda\bar{L}^2 \approx 16$, which might hint at highly aligned dislocations comprising the low-angle grain boundaries left by the extensive shear caused by the plastic flow during the solidification. The *annealed* sample possesses the longest dislocations of the average length of $\bar{L} = 35\,\mu\text{m}$ and a moderate value of $\Lambda\bar{L}^2 \approx 8$, consistent with the expectations that this sample has large grains of size comparable with the sample's diameter $d = 1.1\,\text{mm}$, in which dislocations can be aligned to a certain extent. In contrast, the *cold-worked* sample has shorter dislocations with $\bar{L} = 11.5\,\mu\text{m}$ and $\Lambda\bar{L}^2 = 4$, typical for isotropic volume-filling networks; one might expect that high-amplitude twisting (non-uniform shear deformation in the plane different from that of the shear during growth) causes crossing and multiplication of dislocations—thus producing shorter segments. The *hardened* (by stopping the large-amplitude twisting at $T = 0.03\,\text{K}$) sample is the most puzzling: it has the shortest $\bar{L} = 3\,\mu\text{m}$ (which would not be surprising) but also greatly reduced contribution to the dislocation strain from the gliding dislocations, $\Lambda\bar{L}^2 = 1.3$ (here it is unclear whether the apparent peak in $L^4n(L)$ versus L reflects the actual values of $L^4n(L)$ or it is just an artifact of the onset of the superficial "plateau" due to dislocation yield); in any case, the observable contribution of gliding dislocations is either strongly suppressed or they have become very much shorter than $\sim 2\,\mu\text{m}$, i.e., are outside the range detectable by our apparatus. And the *partially recovered* sample after annealing at 0.60 K is an example of an intermediate state during the restoration of the initially cold-worked and hardened sample eventually all the way back to the annealed state.

Finally, we would like to compute the distributions $L^4n(L)$ using Eqs. 20–21 applied to the temperature dependence of $\epsilon_{\text{dis}}/\epsilon_{\text{el}}$ measured at small strain (Fig. 4), and to compare them with the analysis of an amplitude dependence using Eq. 27,
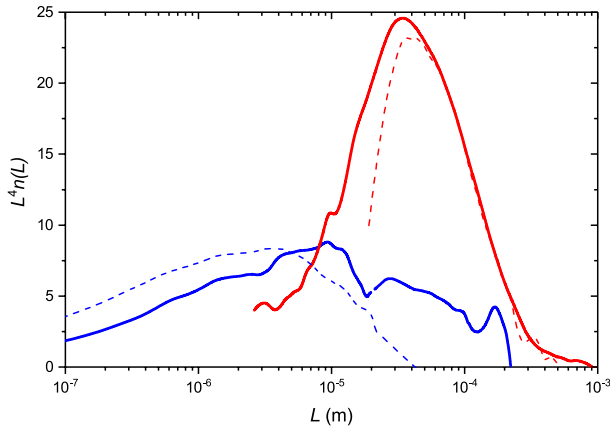
Fig. 8 $L^4 n(L)$ for 'as grown' samples. Blue lines (bob road, $f = 161$ Hz) obtained from temperature sweeps at small amplitudes of strain $\epsilon < 2 \times 10^{-8}$ as in Fig. 4 using Eq. 18 (solid line) and Eq. 19 (dashed) plotted versus the network length $L(T, \omega)$ calculated through Eq. 15. Red lines (solid for the head rod at $f = 931$ Hz, dashed for the bob road at $f = 161$ Hz) are obtained from the amplitude sweeps while decreasing ϵ using Eq. 27, versus the network length $L(\epsilon)$ calculated with Eq. 25 (Color figure online)

presented above. The strain amplitude $\epsilon < 2 \times 10^{-8}$, at which the temperature dependence for the bob rod was taken at $f = 161$ Hz, meets the condition Eq. 14 (provided v_c at our pressure of 51 bar is comparable with $v_c \sim 45\,\mu\text{m s}^{-1}$ measured for $P = 25.3$ bar). Also, the fact that the cross-over temperature for as-grown samples is larger for $f = 931$ Hz than for $f = 161$ Hz (as is expected for $T_\times(f)$ in this regime, Eq. 13) implies that at least the $f = 161$ Hz dataset complies with the condition $v < v_c$. In Fig. 8, we hence plot by blue lines the values of the parameter $L^4 n(L)$ for *as-grown* samples computed using Eq. 18 (solid line) and Eq. 19 (dashed line) versus the network length $L(T)$ calculated through Eq. 15. According to Eqs. 22–23, this method should be valid for L between 0.4 μm and 1.2 mm. And by red lines, $L^4 n(L)$ using Eq. 27, versus the network length L calculated with Eq. 25 (same as in Fig. 7). We can comment that all curves in Fig. 8 demonstrate one broad maximum of comparable (within factor of 2–3) magnitudes at comparable (within factor of 5–10) values of L: the temperature method (blue lines) gives a broad peak of magnitude ~ 8 at $L \sim (6 \pm 2)\,\mu\text{m}$, while the amplitude method gives a peak of magnitude ~ 24 at $L \sim 40\,\mu\text{m}$.

The differences in the positions of peaks most probably arise from the fact that, for both methods, the absolute length scale L is not determined accurately. With the temperature method it enters Eq. 15 through the assumed dependence of the damping parameter $B_3(T)$, measured [2] for $P = 25.3$ bar but not for $P = 53$ bar. And for the amplitude method it relies on the approximate character of Eq. 25. In fact, the length scales in Fig. 7 look a bit overestimated: we would not expect the TO to be sensitive to dislocations longer than some 20% of the sample's radius (~ 0.1 mm)—which contradicts the apparent long-length cut-off for the *annealed* sample of $L_{\max} \sim 0.8$ mm. This implies that lengths L, computed by the amplitude method,

might be overestimated; this is likely to be caused by the approximate character of Eq. 25, as well as by an uncertainty of the absolute value of strain inferred from the twisting angle Θ_1, Eq. 40. With these reservations, we would take the semi-quantitative agreement between the temperature and amplitude methods in Fig. 8 as satisfactory.

4.4 Strain-Hardening and Recovery

Strain amplitudes up to $\epsilon \sim 10^{-7}$ did not affect equilibrium $f_r(T)$ and $f_b(T)$. Increasing ϵ to $\sim 3 \times 10^{-5}$ at $T = 0.3$ K and then cooling to $T \sim 0.02$ K did result in hysteretic amplitude dependences upon reducing and then increasing ϵ; yet this did not lead to any lasting change of sample's rigidity after the temperature was risen back to 0.3 K where the sample would quickly soften again. We associate this regime with binding or unbinding of ^{3}He atoms to the dislocation cores [1, 2]—while dislocations vibrate in the AC strain field in a harmonic way (described by Eq. 3), and their network is kept unchanged. Small additional dissipation was also observed in this regime.

However, straining at amplitudes $\epsilon \geq 8 \times 10^{-5}$ at $T = 0.3$ K resulted in a different behavior. With increasing ϵ the effective shear modulus decreased even further and a substantial additional dissipation appeared—as expected for a now nonlinear response of stretching dislocations. Then, after a prolonged AC-straining with amplitude $\epsilon \sim 10^{-4}$ at 0.3 K (during which the effective shear modulus actually kept increasing slightly and the additional dissipation kept decreasing slightly—perhaps, reflecting gradual hardening of the sample), samples were slowly cooled to 0.03 K (maintaining the soft state with $\mu \approx 0.75\mu_0$), at which the amplitude of twisting was gradually decreased to zero, thus returning to the stiff state with $\mu = \mu_0$ (see Fig. 5). One would then expect that subsequent warming to temperatures $T \gtrsim 0.3$ K while driving at small-amplitude $\epsilon \sim 10^{-8}$ will result in a rapid removal of the trapped ^{3}He and hence restoration of the soft state with $\mu \sim 0.7\mu_0$ (as was routinely observed with other, not strained, samples). In contrast, the stiff state with μ/μ_0 in the range 0.93–0.98 persisted up to ~ 0.5 K, and only a gradual recovery of the soft state could be observed at higher temperatures as shown in Fig. 9 (recovery time of order 1 hour at $T = 1$ K). This phenomenon was originally observed in experiments by John Beamish and colleagues [5, 6]. Furthermore, if such cold-worked samples were only warmed up to 0.3 K and then cooled down to 0.03 K while at a medium-amplitude strain $\epsilon \sim 10^{-5}$, and then the amplitude dependence $\mu(\epsilon)$ while reducing ϵ was measured again, the inferred $L^4 n(L)$ (the "hardened" sample in Fig. 7) was markedly different from the one measured for the first time (the "cold-worked" sample in Fig. 7); the peak in the distribution $L^4 n(L)$ has decreased in magnitude and became shifted to shorter lengths L. Also, the low-amplitude anomalies in $f_r(T)$ and $f_b(T)$ (which we relate to the equilibrium ^{3}He -trapping) were now greatly suppressed.

The rate of the recovery from the *hardened* toward the *soft* state, $f_r(0) - f_r(t)$, was found to have a universal time-dependence [91] as a function of $\ln(1 + t/\tau)$, where $\tau(T) \propto \exp(E_v/k_B T)$ with the activation energy of $E_v \approx 22$ K. In Fig. 9, three different observations of the recovery $\mu(t)/\mu_0$ at temperatures $T_a = 0.55$ K
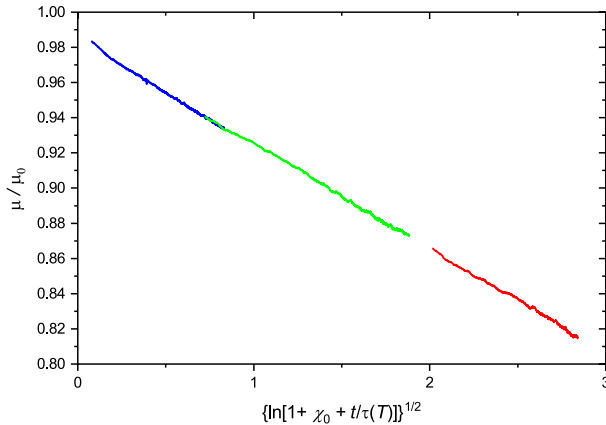
Fig. 9 Time dependence of the softening of the shear modulus during the annealing at constant temperatures $T_a = 0.55$ K (blue), 0.60 K (green), 0.70 K (red), which began at time $t = 0$. It is plotted versus $\ln[1 + \chi_0 + t/\tau(T_a)]$, where $\tau(T) = \tau_D \times \exp(22\,\text{K}/T)$ with $\tau_D = \hbar/(k_B \Theta_D) = 2.4 \times 10^{-13}$ s. The parameter $\chi_0 = \int_{t_1}^{0} \frac{dt}{\tau(T(t))}$ reflects the initial annealing, while the sample was warming up from a low temperature (where $\mu/\mu_0 = 1$) at $t = t_1 < 0$ to T_a; its values are $\chi_0(0.55\,\text{K}) = 0.05$, $\chi_0(0.60\,\text{K}) = 0.7$ and $\chi_0(0.70\,\text{K}) = 60$. The additional bandwidth $f_b - f_b(0) \approx 5 \times 10^{-4}$ Hz was independent of time and temperature (and is relatively insignificant as $Im(\mu)/\mu_0 = 1.2$–1.3%) (Color figure online)

(blue), 0.60 K (green), 0.70 K (red) collapse on a single linear dependence when plotted versus $\ln[1 + \chi(t)]^{1/2}$ in the assumption that a single parameter $\chi = \int_{t_1}^{t} \frac{dt'}{\tau(T(t'))}$ reflects the extent of the recovery of the shear modulus $\mu(t)/\mu_0$ starting from $\mu/\mu_0 = 1$ while at a sufficiently low temperature $T < 0.5\,K$ at time t_1 (for details, see caption for Fig. 9). During the recovery, short dislocations become depleted first, while the largest-scale contribution builds up slower in
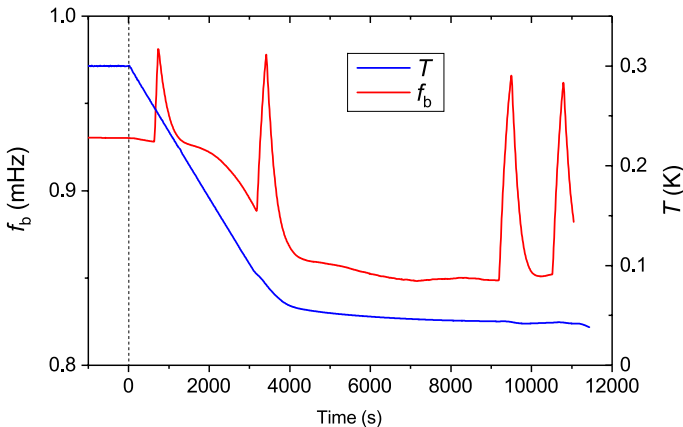

Fig. 10 The history of preparing a sample in the bob rod, kept at a moderate amplitude of twisting with $\epsilon \sim 10^{-5}$, slowly cooled from 0.3 to 0.04 K (typically done at rate 1.5–4 mK/min). The blue and red lines show the temperature and bandwidth f_b, respectively. Occasional spikes in $f_b(t)$ are probably associated with avalanche-like relaxation of the shear stress in the sample (Color figure online)

time (see the evolution from *hardened* through *part-recovered* to *annealed* in Fig. 7).

Occasionally, spikes in the bandwidth f_b (and to a lesser extent in the frequency f_r) of the TO have been observed while at a moderate amplitude of AC-twisting (either at constant temperature or during cooling below 0.3 K), see Fig. 10. These spikes have never been observed at small amplitudes of TO. We hence relate them to a sudden restructuring of the sample, triggered by the AC-strain. These might take form of an avalanche-like motion of many interacting dislocations, similar to those observed at low temperatures [35, 36]—in contrast to the continuous creep at high temperatures. It is believed [32] that a fractal scale-invariant distribution of dislocation cells and dislocation avalanches are consequences of the interaction between dislocations in systems where only glide but no climb is allowed (as in our samples at $T \ll 1$ K).

4.5 Thermal Conductivity

In Fig. 11, by solid symbols we show the thermal conductivity of several samples, converted into the phonon mean free path ℓ with Eq. 42. Black symbols (squares and diamonds for the head and bob road, respectively) are for as-grown samples; blue symbols (up triangles and down triangles for the head and bob road, respectively) are for the samples annealed at $T = 2.0$ K; red stars are for the head sample after it was cold-worked by a high-amplitude AC-twisting. One can see that the phonon m.f.p. was always smaller than that expected for the scattering off rough container walls (Casimir limit), $\ell_{\text{Casimir}} = d = 1.1$ mm. It also varied from sample to sample, decreased after cold working and increased after annealing (following cold-working of the head rod, an overnight annealing at 0.7 K was always returning $\ell(T)$ back to that shown by blue triangles in Fig. 11). Hence, the observed m.f.p. reflects the presence of crystal defects.
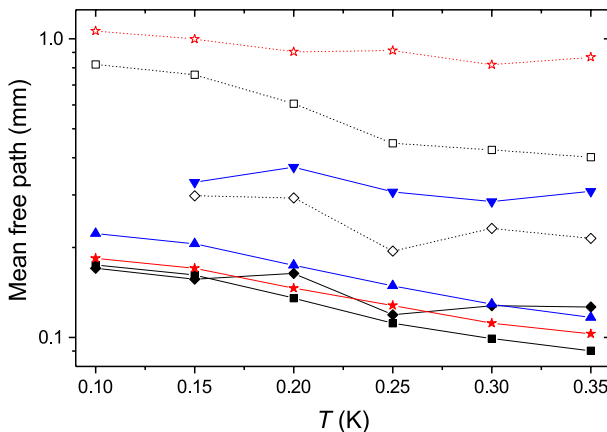

Fig. 11 The effective phonon mean free path of several samples (see text) (Color figure online)

Differences between $\ell(T)$ for the head and bob rod, as well as for the as-grown and cold-worked samples in the head rod might be attributed to different densities and morphologies of dislocation walls in those samples due to the differences in the types of plastic deformation responsible (as the head rod is at the dead end of the common channel, unlike the bob rod, plastic flows during their directed solidification at constant mass and available volume are different; also, straining by AC-twisting would create different types of dislocation structures than during solidification).

To characterize these removable dislocations, we convert, using Eq. 43, the excess in the thermal resistance κ^{-1} into the effective m.f.p. $\ell_{\rm def}$ corresponding to these defects and show it in Fig. 11 by open symbols connected by a dotted line of the same color (square and diamond for the as-grown defects in the head and bob road, respectively) and by red stars for the defects introduced by cold working. Similar to the case of total $\ell(T)$, the temperature dependence of $\ell_{\rm def}(T)$ is either rather weak or basically absent. Such $\ell_{\rm def} \sim 1$ mm cannot be due to a homogeneous network of non-interacting fluttering dislocations: while these dislocations of length $L \lesssim 20$ nm would indeed result in a flat $\ell_{\rm def}(T)$—but with $\ell_{\rm def} \sim L \sim 20$ nm (Eq. 34), not 1 mm; and dislocations of larger length $L \sim 10\,\mu$m would be able to make $\ell(T) \sim 1$ mm but with a different temperature dependence $\ell \propto T$ (Eq. 35). Isolated static dislocations should also be discarded as they would produce a different temperature dependence $\ell \propto T^{-1}$ (Eq. 36), and would have to be of a very short length $L \sim 30$ nm—at which flutter would become dominant anyway. However, the static strain field due to large-angle grain boundaries or, more likely, collective strain field of dislocation walls is consistent with the observed temperature dependence and values of $\ell_{\rm def}(T)$ if the size of such grains or dislocation cells is $\xi \lesssim 0.3$ mm (Eq. 37)—which seems natural for a rod-shaped sample of diameter $d = 1.1$ mm.

5 Discussion

It seems, the observed dynamics of different samples of polycrystalline ^{4}He, at strain amplitudes not exceeding that for plastic yield, could be consistently interpreted in terms of the Granato–Lücke theory of vibrating dislocations. However, the process of AC-straining at high amplitudes, followed by the apparent disappearance of gliding dislocations after stopping this straining at a low temperature, warrants a discussion.

At low temperatures, the increase of the shear modulus to its stiff value means that either the volume fraction of gliding basal-plane dislocations has been drastically reduced or that certain interactions stop most of them from gliding. In the case of an equilibrium state without straining by high-amplitude shear, this mechanism is believed to be the condensation of ^{3}He atoms on the dislocation cores, which can be then quickly reversed by warming up to 0.3 K. We would speculate that, in the highly metastable *hardened* state, the dislocations are stopped from gliding by some novel mechanism which works even at $T = 0.3$ K at which ^{3}He atoms should have mostly evaporated from dislocation cores.

It is evident from Fig. 7 that cold working by high TO amplitude $\epsilon \sim 10^{-4}$ creates many short dislocations at expense of long ones. During 10 hours of straining,

the resonant frequency f_r kept increasing slowly from the lowest value typical to the annealed samples while the bandwidth f_b was only slightly greater than that for a stiff crystal. The relatively low level of damping suggests that all dislocations longer than $L_{max}(\epsilon)$ have been eliminated, and the stress–strain cycles are quasi-elastic (i.e., no longer hysteretic). The relatively low value of μ indicates the presence of a volume-filling network of gliding dislocations. And the slow increase of μ is an evidence for some process of immobilization of these gliding dislocations, unrelated to the condensation of ^{3}He atoms (as the temperature is too high for this process).

We can speculate that, during a continuous AC straining at high amplitude, this system is kept in a dynamical state, in which stretching dislocations are mostly aligned [31] (which prevents them from crossings and creating jogs), thus maintaining a soft state with an agile response of gliding dislocations to the rapidly alternating high strain. However, upon stopping the agitation, the dislocation network relaxes irreversibly, thus creating crossings and jogs which nearly completely arrest the glide of dislocations—with or without ^{3}He atoms in their cores. This is why the subsequent un-trapping of ^{3}He atoms after warming up to $T = 0.3$ K does not help to soften the crystal. And only a higher-temperature annealing can remove those jogs and restore free glide with its greatly reduced shear modulus.

We conclude that the hardening of strained sample (while the strain amplitude was being decreased at $T = 0.03$ K), should be related to the immobilization of gliding dislocations by hard topological defects like jogs or by reducing their volume fraction through the creation of structures like dislocation walls—and the recovery from this state at elevated temperatures takes much longer than the quick thermally activated un-trapping and ballistic removal of ^{3}He quasiparticles. The time dependence of the recovery with the activation energy of ~ 22 K hints at the annealing of these defects via dislocation climb facilitated by the mass transport of ^{4}He, presumably controlled by thermal vacancies.

There might be alternative explanations of the slow relaxation of *hardened* samples at $T = 0.3$ K. Firstly, it could be that the normally dominant mass transport of ^{4}He atoms, required to remove jogs, is maintained via 1-D dislocations; it can hence be suppressed by the presence of ^{3}He-contaminated nodes (with larger trapping energy of 1–2 K) [19]. Then, after the dislocation network length was reduced by cold-working, the number of these nodes increased: this would greatly lengthen the time needed for the diffusive transport of ^{4}He atoms through them. Secondly, in a work-hardened sample ^{3}He atoms could become localized in the regions of high strain, so their transport is no longer through the quantum diffusion of ballistic quasiparticles but through the vacancy-assisted hopping. Then, ^{3}He atoms would not be effectively leaving dislocation cores, thus retaining the sample in the stiff state for much longer even at $T \sim 0.3$ K.

An argument in favor of collective behavior of interacting gliding dislocations can be made from the thermal conductivity of our samples. The temperature dependence of $\ell(T)$ (either absent or weakly decreasing at best—similar to those observed in samples of hcp ^{4}He and bcc ^{3}He, grown by the same technique [3, 4]) is consistent with the predominant scattering of phonons not off individual vibrating dislocations but off either grain boundaries (which in samples grown by a blocked-capillary method could be expected to be a distance $\sim d$ apart) or dislocation walls

(i.e., regions filled with dense arrays of polarized dislocations surrounding dislocation-free regions—dislocation cells). These dislocation walls are different from grain boundaries in several respects [32]: the misalignment of internal regions of these cells is much less pronounced than in polycrystalline grains; they are more fuzzy than the better defined grain boundaries; in crystals where only easy glide but not climb of dislocations is allowed, these cells were found to be organized in a self-similar way over a broad range of length scales; finally, it is dislocations (even though tangled together) and not grain boundaries—which can be effectively annealed at moderate temperatures which unleash dislocation climb. The observed recovery of the thermal conductivity upon annealing at the relatively low temperature of 0.7 K (as compared to the melting temperature of 2.4 K, usually required for the efficient annealing of grain boundaries) indicates that it is dislocations but not grain boundaries which are being eliminated and restructured. Finally, the observed sporadic avalanche-like relaxation of stress at low temperatures is also consistent with the collective behavior of dislocations arranged in complex structures.

6 Summary

1. The distribution $L^4 n(L)$ was measured, using low-temperature amplitude sweeps [1, 2] for different samples of solid helium: as-grown, annealed, cold-worked, hardened and recovered. Thus, changes in the main parameters characterizing the density ($\bar{L}$ and Λ) and connectivity ($\Lambda \bar{L}^2$) of the networks of gliding dislocation were studied. All samples (except for the *hardened* one) revealed single peaks in $L^4 n(L)$ of comparable width but varying position and height, implying single-scale distributions characterized by particular values of $\bar{L}$ and $\Lambda \bar{L}$. The apparent *plateau* at shorter lengths of order $\sim L_{min}$ is most likely an artifact when required strain amplitude $\epsilon_{c2}(L_{min})$ exceeded $\epsilon_{c3}(L_{max})$, causing stretching of the longest dislocations.

2. We verified experimentally a method of determining the length distribution $L^4 n(L)$ from the equilibrium temperature dependence of either real or imaginary part of the shear modulus μ at small amplitudes of shear strain—by accounting for the dissipative drag due to the equilibrium density of trapped ^{3}He impurities [2]. The results are qualitatively consistent with those from the accepted method using the non-equilibrium amplitude dependence of $\mu(\epsilon)$ while reducing strain amplitude ϵ. Further work is required to refine the calibration of lengths and general accuracy of this method.

3. The process [6] of eliminating the dislocation glide by decreasing the strain amplitude at low temperature and its subsequent slow recovery at temperatures above 0.5 K was investigated. Short dislocations, created by high-amplitude cold working, and whose motion is then arrested by either topological network anchors (like jogs) or interacting dislocation structures (like dislocation walls), can be gradually freed by annealing at a moderate temperature of ~ 0.6 K—unlike the dislocations introduced during the sample growth, which (along, perhaps, with some grain boundaries) could only be partially annealed at temperature as high as 1.8 K. An overnight annealing at 0.7 K (or 1 h at 1.0 K) completely removes these short immobilized dislocations created by cold-working and re-introduces long gliding ones,

eventually restoring the soft state of the crystal. This is correlated with the process of the recovery of thermal conductivity, sensitive to the presence of dislocation walls. The temperature-dependent relaxation time, controlling the universal logarithmic time-dependence of the recovery, has the activation energy of 22 K pointing at the possible role of thermal vacancies in mass transport.

4. Measurements of thermal conductivity, which characterizes the mean free path of transverse phonons [4] as function of temperature and treatment, indicated that the model of homogeneous volume-filling network of non-interacting dislocations is inadequate. Most likely, there are both grain boundaries and dislocation cells of size, comparable with the diameter of the sample; the latter being introduced by cold-working and are effectively removed at moderate temperatures ~ 0.6 K.

5. Occasional dislocation avalanches [35] were observed at temperatures below 0.3 K in samples subjected to a moderate-amplitude AC strain during cooling. This is consistent with theories [32] proposing the creation of fractal dislocation cells after plastic deformation of crystals with easy glide but no climb of edge dislocations.

References

1. I. Iwasa, J. Low Temp. Phys. **171**, 30 (2013)
2. A.D. Fefferman, F. Souris, A. Haziot, J.R. Beamish, S. Balibar, Phys. Rev. B **89**, 014105 (2014)
3. A.S. Greenberg, G.A. Armstrong, Phys. Rev. B **20**, 1049 (1979)
4. G.A. Armstrong, A.A. Helmy, A.S. Greenberg, Phys. Rev. B **20**, 1061 (1979)
5. J. Day, O. Syshchenko, J. Beamish, Phys. Rev. B **79**, 214524 (2009)
6. J. Beamish, J.P. Franck, Phys. Rev. B **26**, 6104 (1982)
7. A. Granato, K. Lücke, J. Appl. Phys. **27**, 583 (1956)
8. J. Friedel, *Dislocations* (Pergamon, New York, 1964)
9. J. Hirth, J. Lothe, *Theory of Dislocations* (Krieger Publishing Company, Malabar, 1964)
10. J. Beamish, J. Low Temp. Phys. **197**, 187 (2019)
11. J. Beamish, S. Balibar, Rev. Mod. Phys. **92**, 045002 (2020)
12. A.F. Andreev, I.M. Lifshitz, Sov. Phys. JETP **29**, 1107 (1969)
13. A. Haziot, X. Rojas, A.D. Fefferman, J.R. Beamish, S. Balibar, Phys. Rev. Lett. **110**, 035301 (2013)
14. E.J.L. Borda, W. Cai, M. de Koning, Phys. Rev. Lett. **117**, 045301 (2016)
15. These dislocations are made of stacking-fault ribbons between two parallel Schottky partial dislocations separated by ~ 400 Å[14]

16. J. Day, J. Beamish, Nature **450**, 853 (2007)
17. G.A. Kneezel, A.V. Granato, Phys. Rev. B **25**, 2851 (1982)
18. S.I. Shevchenko, Fiz. Nizk. Temp. **13**, 115 (1987)
19. M.H.W. Chan, J. Low Temp. Phys. **205**, 235 (2021)
20. J. Shin, M.H.W. Chan, Phys. Rev. B **101**, 014507 (2020)
21. Z.G. Cheng, J. Beamish, Phys. Rev. Lett. **117**, 025301 (2016)
22. Z.G. Cheng, J. Beamish, Phys. Rev. Lett. **121**, 225304 (2018)
23. M.W. Ray, R.B. Hallock, Phys. Rev. Lett. **100**, 235301 (2008)
24. S.G. Soyler, A.B. Kuklov, L. Pollet, N.V. Prokof'ev, B.V. Svistunov, Phys. Rev. Lett. **103**, 175301 (2009)
25. A. Vilenkin, E.P.S. Shellard, *Cosmic Strings and Other Topological Defects* (Cambridge University Press, Cambridge, 1994)
26. C.J.A.P. Martins, *Defect Evolution in Cosmology and Condensed Matter: Quantitative Analysis with the Velocity-Dependent One-Scale Model* (Springer, Berlin, 2016)
27. L.H. Nosanow, W.J. Titus, J. Low Temp. Phys. **1**, 73 (1969)
28. R.P. Feynman, Prog. Low Temp. Phys. **1**, 17 (1955)
29. W.F. Vinen, Proc. Roy. Soc. A **242**, 493 (1957)
30. P.M. Walmsley, A.I. Golov, Phys. Rev. Lett. **118**, 134501 (2017)
31. E. Varoquaux, Phys. Rev. B **86**, 064524 (2012)
32. J.P. Sethna, Annu. Rev. Mater. Res. **47**, 217 (2017)
33. H. Mughrabi, T. Ungár, W. Kienle, M. Wilkens, Philos. Mag. A **53**, 793 (1986)
34. B. Bakó, W. Hoffelner, Phys. Rev. B **76**, 214108 (2007)
35. Z.G. Cheng, J. Beamish, Phys. Rev. Lett. **121**, 055301 (2018)
36. M.A. Lebyodkin, I.V. Shashkov, T.A. Lebedkina, K. Mathis, P. Dobron, F. Chmelik, Phys. Rev. E **88**, 042402 (2013)
37. A.H. Cottrell, in *Dislocations in Solids* edited by F. R. N. Nabarro and M. S. Duesbery, **11**, vii-xvii, Elsevier 2002
38. R.P. Feynman, R.B. Leighton, M. Sands, *The Feynman lectures on physics*, vol. 1 (Addison-Wesley, New York, 1964)
39. M.A. Paalanen, D.J. Bishop, H.W. Dail, Phys. Rev. Lett. **46**, 664 (1981)
40. V.L. Tsymbalenko, Z. Eksp, Teor. Fiz. **74**, 1507 (1978)
41. V.L. Tsymbalenko, Sov. Phys. JETP **47**, 787 (1978)
42. V.L. Tsymbalenko, Z. Eksp, Teor. Fiz. **76**, 1690 (1979)
43. V.L. Tsymbalenko, Sov. Phys. JETP **49**, 859 (1979)
44. F. Tsuruoka, Y. Hiki, Phys. Rev. B **20**, 2702 (1979)
45. Yu. Mukharsky, A. Penzev, E. Varoquaux, Phys. Rev. B **80**, 140504(R) (2009)
46. Y. Mukharsky, A. Penzev, J. Low Temp. Phys. **169**, 197 (2012)
47. R. Wanner, I. Iwasa, S. Wales, Solid State Commun. **18**, 853–856 (1976)
48. I. Iwasa, H. Kojima, Phys. Rev. B **102**, 214101 (2020)
49. I. Iwasa, K. Araki, H. Suzuki, J. Phys. Soc. Jpn. **46**, 1119 (1979)
50. Y. Aoki, I. Iwasa, T. Miura, A. Yamaguchi, Y. Okuda, J. Low Temp. Phys. **183**, 113–119 (2016)
51. A.A. Levchenko, L.P. Mezhov-Deglin, Zh. Eksp. Teor. Fiz. **86**, 2123–2133 (1984)
52. A.A. Levchenko, L.P. Mezhov-Deglin, Sov. Phys. JETP **59**, 1234–1240 (1984)
53. D.E. Zmeev, A.I. Golov, Phys. Rev. Lett. **107**, 065302 (2011)
54. D.E. Zmeev, M.Y. Brazhnikov, R. Schanen, A.I. Golov, J. Low Temp. Phys. **169**, 169–179 (2012)
55. M.Y. Brazhnikov, D.E. Zmeev, A.I. Golov, Fizika Nizkikh Temperature (Sov. Low Temp. Phys) **38**, 1329–1335 (2012)
56. M.Y. Brazhnikov, D.E. Zmeev, A.I. Golov, Low Temp. Phys. **38**, 1049–1054 (2012). https://doi.org/10.1063/1.4765093
57. E. Kim, M.H.W. Chan, Science **305**, 1941 (2004)
58. E. Kim, M.H.W. Chan, Nature **427**, 225 (2004)
59. Y. Aoki, J.C. Graces, H. Kojima, Phys. Rev. Lett. **99**, 015301 (2007)
60. J.D. Reppy, Phys. Rev. Lett. **104**, 255301 (2010)
61. J.D. Reppy, X. Mi, A. Justin, E.J. Mueller, J. Low Temp. Phys. **168**, 175–193 (2012)
62. V. Gadagkar, E.J. Pratt, B. Hunt, M. Yamashita, M.J. Graf, A.V. Balatsky, J.C. Davis, J. Low Temp. Phys. **169**, 180–196 (2012)

63. I. Iwasa, Phys. Rev. B **81**, 104527 (2010)
64. S. Balibar, J. Beamish, A. Fefferman, A. Haziot, X. Rojas, F. Souris, C. R. Physique **17**, 264–275 (2016)
65. X. Rojas, A. Haziot, V. Bapst, S. Balibar, H.J. Maris, Phys. Rev. Lett. **105**, 145302 (2010)
66. J.D. Eshelby, Proc. R. Soc. Lond. A **266**, 222 (1962)
67. F. Souris, A.D. Fefferman, H.J. Maris, V. Dauvois, P. Jean-Baptiste, J.R. Beamish, S. Balibar, Phys. Rev. B **90**, 180103(R) (2014)
68. T. Ninomiya, J. Phys. Soc. Jpn. **36**, 399 (1974)
69. A.V. Markelov, Z. Eksp, Teor. Fiz. **88**, 205 (1985)
70. A.V. Markelov, Sov. Phys. JETP **61**, 118 (1985)
71. A. Haziot, A.D. Fefferman, F. Souris, J.R. Beamish, H.J. Maris, S. Balibar, Phys. Rev. B **88**, 014106 (2013)
72. Note that the prefactor in Eq. 7 agrees with that in the original paper [7] but is a factor of $\pi/2 = 1.57$ greater than that quoted in papers [2, 11]. This affects the value of α in Eq. 9 and hence calibration of $L^4 n(L) \propto \alpha^{-1}$, calculated from experimental data using Eqs. 20, 21 and 27
73. J.A. Garber, A.V. Granato, J. Phys. Chem. Solids **31**, 1863 (1970)
74. One may assume that E_b scales with pressure as $E_b \propto \mu(P_m)\Delta V_{34}$, where μ is the shear modulus and ΔV_{34} is the difference in molar volumes of hcp ^{3}He and ^{4}He at pressure corresponding to distance $\sim b$ from the dislocation core [9], $P_m - \frac{\mu}{3\pi}\frac{1+\nu}{1-\nu} \approx P_m - 0.20\mu(P_m)$). With increasing P_m from 25.3 bar to our pressure of 53 bar: μ increases by factor of 1.50 while ΔV_{34} drops by factor of ~ 1.3
75. W. Voigt, *Lehrbuch der Kristallphysik* (Teubner, Leipzig, 1928)
76. A. Reuss, Angew. Math. Mech. **9**, 55 (1929)
77. R. Hill, Proc. Phys. Soc. A **65**, 349 (1952)
78. H.J. Maris, S. Balibar, J. Low Temp. Phys. **160**, 5 (2010)
79. D.S. Greywall, Phys. Rev. B **16**, 5127 (1977)
80. R.H. Crepeau, O. Heybey, D.M. Lee, S.A. Strauss, Phys. Rev. A **3**, 1162 (1971)
81. E.R. Grilly, R.L. Mills, Ann. Phys. (N.Y.) **18**, 250 (1962)
82. I. Iwasa, H. Kojima, J. Low Temp. Phys. **187**, 459 (2017)
83. A.C. Anderson, M.E. Malinowski, Phys. Rev. B **5**, 3199 (1972)
84. P.G. Klemens, Proc. Phys. Soc. Lond. A **68**, 1113 (1955)
85. P.G. Klemens, in Solid State Physics, edited by F. Seitz and D. Turnbull (Academic, New York, 1958), **7**, 1
86. D.J. Bishop, J.D. Reppy, Phys. Rev. B **22**, 5171 (1980)
87. A single-frequency TO of this type was used by Paalanen *et al.* [39] in their pioneering studies of low-frequency internal friction due to moving dislocations in solid helium
88. J.R. Hook, E. Faraj, S.G. Gould, H.E. Hall, J. Low Temp. Phys. **74**, 45 (1989)
89. Thanks to the $\propto r^4$ contribution to the rigidity of a rod of solid helium at radius r, the dominant contribution to the measured μ comes from the thin sheath of effective thickness ~ 0.1–0.2 mm (for either 50% or 90% of total μ, respectively) near the rim
90. J.M. Ziman, *Electrons and Phonons* (Oxford University Press, Oxford, 2001)
91. This type of relaxation was documented for creep in igneous rocks [92] but was then commonly observed in various polycrystals including solid helium [51, 52]
92. C. Lomnitz, J. Geol. **64**, 473 (1956)

Authors and Affiliations

M. Yu. Brazhnikov[1,2] · Y. M. Mukharsky[3] · A. I. Golov[1]

✉ A. I. Golov
andrei.golov@manchester.ac.uk

1   Department of Physics and Astronomy, The University of Manchester, Manchester M13 9PL,
     UK

2   Institute of Solid State Physics, Chernogolovka, Russia 142432

3   Department of Condensed Matter Physics, CEA-Saclay/IRAMIS, 91191 Gif sur Yvette, Cedex,
     France